TUDelft

Delft University of Technology

Locally optimal control laws for Earth-bound solar sailing with atmospheric drag

Carzana, Livio; Visser, Pieter; Heiligers, Jeannette

Important note
To cite this publication, please use the final published version (if applicable).
Please check the document version above.

Locally optimal control laws for Earth-bound solar sailing with atmospheric drag

Livio Carzana *, Pieter Visser, Jeannette Heiligers

Faculty of Aerospace Engineering, Delft University of Technology Kluyverweg 1, 2629 HS Delft, the Netherlands

ARTICLE INFO

ABSTRACT

Solar sailing is a spacecraft propulsion method relying solely on solar radiation pressure to provide thrust and is therefore propellantless by nature. Although it represents a practical and promising propulsion system particularly suited for heliocentric flight regimes, the majority of sailcraft missions flown to date have remained Earth-bound and more Earth-bound missions are scheduled for the near future. However, the fundamental dynamics and trajectory optimization of a solar sail around the Earth have only been investigated to a limited extent, often neglecting the effect of non-negligible perturbations in the dynamics and the optimal control problem. Among these perturbations are the effect of eclipses, non-spherical gravity, and aerodynamic drag. Their magnitude can be comparable to, or even exceed that of solar radiation pressure and their effect on the solar-sail dynamics should be investigated to ensure the sailcraft's transfer capabilities and controllability. This article does so by including these perturbations in the dynamics and by considering aerodynamic drag in the optimal control problem. Using this formulation, it is shown that the optimal control problem is independent of the solar-sail loading parameter and that, by solving it, locally optimal steering laws can be derived to effectively change individual orbital elements. These newly derived steering laws form an extension to the laws found by McInnes for unperturbed solar-sail Earth-bound motion. By accounting for the perturbations in the derivation of the steering laws, it is possible to characterize how the perturbations affect the solar-sail maneuvering capabilities. This is quantified based on the established increase of the targeted orbital element. Furthermore, a range of different starting orbits will be considered to analyze the effects of perturbations in different orbital regimes. As demonstration of the real need for this investigation, NASA's Advanced Composite Solar Sail System (ACS3) mission will be considered as real-case scenario. This mission is scheduled for launch in mid-2022 and may benefit from the steering laws derived in this article to prove the maneuverability of solar sails in Earth orbit.

1. Introduction

The usage of solar sails as main propulsion system for spaceflight applications is an idea that was first investigated at the beginning of the last century and has since drawn increasingly more attention worldwide [1]. The research interest in solar sailing, initially within the scientific community and later also within space agencies, is mainly driven by its propellantless nature. In the last decades many studies on solar sailing demonstrated its applicability to a wide variety of mission scenarios, ranging from interplanetary and interstellar missions to planet-centered ones [2,3]. Analyses of solar-sail interplanetary and deep-space trajectories have clearly shown the mission-enabling potential of solar sails and,

in particular, the promising thrusting capabilities when approaching the inner Solar System, where solar radiation pressure (SRP) is particularly strong and an improved sailcraft maneuverability is achieved [3,4]. While the majority of research works indeed focus on interplanetary solar-sail mission applications, most solar-sail missions launched to date have flown solely in low Earth orbit (LEO). Their purpose was to either show the feasibility of solar-sail deorbiting (e.g., NASA's NanoSail-D2 mission [5,6]), the successful control of SRP as propulsive means, or the advancements in sail manufacturing and deployment capabilities (e.g., The Planetary Society's LightSail 1 and LightSail 2 [7,8]). In a similar fashion, other near-future solar-sail missions, including NASA's Advanced Composite Solar Sail System (ACS3) mission, will also be launched in LEO and act as sail technology and orbit control demonstrator [9].

Although solar-sail technology demonstrators have been flown mostly in LEO, thus far the research conducted on planetocentric solar-sail orbital dynamics and control is very limited. Several

* Corresponding author.
E-mail address: L.Carzana@tudelft.nl (L. Carzana).

Nomenclature

Abbreviations

ACS3	Advanced Composite Solar Sail System
AE	Acceleration envelope
ECI	Earth-centered inertial
EoM	Equations of motion
IDW	Inverse distance weighted
LEO	Low Earth orbit
LTAN	Local time of the ascending node
NpS	Nodes per orbital segment
POINT	Pre-run Optimization and in-run INTerpolation
RMS	Root mean square
SMA	Semi-major axis
SpO	Segments per orbit
SRP	Solar radiation pressure

Notation

$\boldsymbol{x}$	Vector
x	Scalar/Norm of vector
$\hat{\Box}$	Unit vector/Direction
$\overline{\Box}$	Averaged/Normalized
$\dot{\Box}$	First-order time derivative
$\ddot{\Box}$	Second-order time derivative
$\|\Box\|$	Norm of vector
$\Delta\Box$	Difference
$\circ$	Hadamard product

Variables

$\boldsymbol{a}$	Acceleration vector
a	Semi-major axis
a_c	Solar-sail characteristic acceleration
C_D	Drag coefficient
C_L	Lift coefficient
c	Speed of light in vacuum
$\boldsymbol{D}$	Aerodynamic drag
$\hat{\boldsymbol{d}}$	Projection of $\hat{\boldsymbol{n}}$ onto $(\hat{\boldsymbol{y}}_S, \hat{\boldsymbol{z}}_S)$ plane
e	Eccentricity
$\hat{\boldsymbol{h}}$	Orbital momentum unit vector
h	Altitude
i	Inclination
J	Cost function
J_2	Spherical harmonics coefficient
$\boldsymbol{L}$	Aerodynamic lift
$\mathcal{N}$	Optimal normal direction matrix
N	Number of grid points
$\hat{\boldsymbol{n}}$	Solar-sail normal direction
O	Reference frame
P	Orbital period
$\hat{\boldsymbol{p}}$	Auxiliary vector
R	Acceleration ratio
$\boldsymbol{r}$	Sailcraft position vector
$\boldsymbol{S}$	Optimization set
$S_{\oplus}$	Solar flux at Earth
$\hat{\boldsymbol{s}}$	Sunlight direction
T	Runtime

t	Time
$\boldsymbol{u}$	Control vector
V_R	Atmospheric particle velocity ratio
$\boldsymbol{v}$	Sailcraft inertial velocity
$\boldsymbol{w}$	Weight vector
$\boldsymbol{X}$	Sailcraft state
x, y, z	Cartesian coordinates
α	Solar-sail cone angle
Γ	Set of pre-optimized normal directions
γ, ζ, ξ, χ	Angular coordinates of the solar-sail normal direction
δ	Solar-sail clock angle
ϵ	Error
ε	Angle between drag direction and tangent to the acceleration envelope curve
η	Angle between the drag and sunlight directions
θ, ϕ	Spherical coordinates of the primer vector
ϑ	True anomaly
Λ	Full-dynamics optimization angle
$\boldsymbol{\lambda}$	Primer vector
$\mu_{\oplus}$	Earth's gravitational parameter
ν	Shadow parameter
ρ	Atmospheric density
$\boldsymbol{\varrho}$	Vector of inverses of the Euclidean distance
Σ	Set of pre-optimized grid points
σ	Solar-sail loading parameter
σ_N, σ_T	Aerodynamic momentum accommodation coefficients
$\hat{\boldsymbol{\tau}}$	Direction tangent to the acceleration envelope curve
ψ	Angle between the drag and aerodynamic acceleration
Ω	Right ascension of the ascending node
ω	Argument of perigee

Subscripts

0	Initial
abs	Absolute
aero	Aerodynamic
I	Inertial frame
J2	J_2 spherical harmonics coefficient
k	Generic k^{th} vector component
max	Maximum
min	Minimum
NBH	Neighboring
n	Solar-sail normal
O	Optimization frame
ref	Reference
rel	Relative
S	Sunlight frame
SRP	Solar radiation pressure
t	Target
V	Velocity frame

Superscripts

*	Optimal
'	Derivative
+, −	Neighboring grid points
T	Transpose

studies on the topic are based on the solar-sail control laws first devised by McInnes [1], valid for simplistic, perfectly reflecting solar sails with either unperturbed two-body problem dynamics or gravitational perturbations only. Applications of such control laws range from the analysis of planetocentric solar-sail trajectories [10,11] to the study of Earth-escape strategies [12–14]. When considering also non-gravitational perturbations in the analysis of Earth-bound solar-sail trajectories an increased degree of complexity is achieved, which stems from the highly nonlinear dynamics to be considered. Indeed, perturbing accelerations such as the planetary radiation pressure and aerodynamic accelerations can achieve magnitudes comparable to – or even greater than – the SRP acceleration, therefore making the dynamics deviate substantially from the ones of the two-body problem with ideal SRP acceleration. As a consequence, results found with the latter dynamics have limited applicability in the analysis of high-fidelity solar-sail trajectories. Preliminary studies on perturbed, Earth-bound sailcraft trajectories have been proposed only in small numbers, with particular focus on the analysis of the coupled effects of SRP and planetary radiation pressure for Earth-centered orbits [15,16], studies on SRP and aerodynamics-based optimal control laws for orbit raising and maneuvering [17–20], and the analysis of the drag-induced active debris removal and deorbiting capabilities of solar sails [21–24]. The highly-nonlinear dynamical models considering the effects of planetary radiation pressure and/or aerodynamics significantly complicate the computation of optimal steering laws. Consequently, the methods and results proposed are valid only under simplifying assumptions (e.g., on the orbit shape and its orientation with respect to the Sun's position) and for orbit raising and inclination change steering laws only.

As a first step towards a generic, high-fidelity solar-sail planetocentric optimal control solver, this article proposes a novel technique to efficiently and accurately optimize Earth-bound solar-sail trajectories in the presence of SRP, gravitational perturbations, and aerodynamic drag. Unlike all other methods employed to date to solve this optimization problem, the one proposed here can be used for any steering law and applied to any orbital regime. This first-of-its-kind technique is based on the idea of pre-solving the optimization problem for a wide set of conditions and to interpolate the optimal solutions found during the trajectory propagation. In this work, this optimization technique is described in its entirety, with focus on its accuracy and limited runtime. NASA's upcoming ACS3 mission is taken as a specific and realistic test case. The ACS3 mission will be launched into a 715 km altitude Sun-synchronous orbit. The results in this article will demonstrate the sailcraft's ability to change its orbital altitude and inclination. However, also more generic analyses on applicable steering laws and orbital altitudes are provided, though limited to Sun-synchronous orbits. This class of orbits is selected to reduce the design space, justified by the fact that this class is often used for Earth-centered scientific missions. Nevertheless, the designed novel optimization method presented in this work is applicable to any steering law and orbital regime. Hence, this article significantly contributes to the body of knowledge on optimal solar-sail control laws in the near-Earth environment.

2. Dynamical model

In this section the dynamical model used throughout this article is presented. First, different reference frames and coordinate systems are defined and subsequently the sailcraft equations of motion (EoM) are provided.
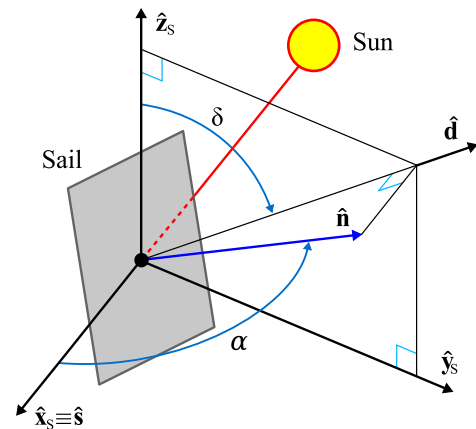
Fig. 1. Sailcraft normal direction and attitude angles in the sunlight reference frame, $O_S(\hat{\boldsymbol{x}}_S, \hat{\boldsymbol{y}}_S, \hat{\boldsymbol{z}}_S)$.

2.1. Reference frames and coordinate systems

In the following sections, different reference frames and coordinate systems are presented to conveniently express the sailcraft dynamics and optimization problem under investigation.

2.1.1. Earth-centered inertial reference frame

The Earth-centered inertial (ECI) reference frame is the frame in which the sailcraft EoM are propagated. This frame is indicated by $O_I(\hat{\boldsymbol{x}}_I, \hat{\boldsymbol{y}}_I, \hat{\boldsymbol{z}}_I)$ and is centered at the Earth's center of mass, with the $\hat{\boldsymbol{x}}_I$-axis pointing towards the mean vernal equinox at January 1st, 2000, the $\hat{\boldsymbol{z}}_I$-axis pointing perpendicular to the mean equatorial plane at January 1st, 2000 (towards the Northern hemisphere), and the $\hat{\boldsymbol{y}}_I$-axis completing the right-handed frame. Within frame O_I, a Cartesian coordinate system is used, identified by the coordinates x_I, y_I, and z_I.

2.1.2. Sunlight reference frame

The sunlight reference frame is a sailcraft-centered frame indicated by $O_S(\hat{\boldsymbol{x}}_S, \hat{\boldsymbol{y}}_S, \hat{\boldsymbol{z}}_S)$, see Fig. 1. The $\hat{\boldsymbol{x}}_S$-axis points in the Sun-to-sailcraft direction (i.e., parallel to the direction of sunlight), $\hat{\boldsymbol{s}}$, $\hat{\boldsymbol{y}}_S = \hat{\boldsymbol{z}}_I \times \hat{\boldsymbol{s}}$, and the $\hat{\boldsymbol{z}}_S$-axis completes the right-handed frame. Since a flat solar-sail model is considered in this work (see Section 2.2.1 for more details), the sailcraft orientation is uniquely determined by the sail normal direction, $\hat{\boldsymbol{n}}$. By making use of a spherical coordinate system, $\hat{\boldsymbol{n}}$ can be defined by two attitude angles: the cone angle α, defined as the angle between the direction of sunlight, $\hat{\boldsymbol{s}}$, and the sail normal direction, $\hat{\boldsymbol{n}}$, and the clock angle δ, measured from the $\hat{\boldsymbol{z}}_S$ direction to the projection of the sail normal onto the $(\hat{\boldsymbol{y}}_S, \hat{\boldsymbol{z}}_S)$ plane, $\hat{\boldsymbol{d}}$ (see Fig. 1). Commonly, only one side of the solar sail can be exposed to direct sunlight. Hence, in this article it is assumed that the sail normal has no component pointing towards the Sun, i.e., $\alpha \in [0, \pi/2]$ and $\delta \in [0, 2\pi]$. The sail normal expressed in the sunlight frame, $\hat{\boldsymbol{n}}_S$, is then found as:

$$\hat{\boldsymbol{n}}_S = \cos\alpha\,\hat{\boldsymbol{x}}_S + \sin\alpha\sin\delta\,\hat{\boldsymbol{y}}_S + \sin\alpha\cos\delta\,\hat{\boldsymbol{z}}_S \tag{1}$$

2.1.3. Velocity reference frame

The velocity reference frame $O_V(\hat{\boldsymbol{x}}_V, \hat{\boldsymbol{y}}_V, \hat{\boldsymbol{z}}_V)$, see Fig. 2, is centered at the sailcraft center of mass and has its $\hat{\boldsymbol{x}}_V$-axis pointing along the direction of the inertial velocity, $\hat{\boldsymbol{v}}$, the $\hat{\boldsymbol{z}}_V$-axis parallel to the satellite's orbital momentum vector, $\hat{\boldsymbol{h}}$, and the $\hat{\boldsymbol{y}}_V$-axis such that it forms a right-handed frame. By using a spherical coordinate system, the sail normal direction, $\hat{\boldsymbol{n}}$, can be uniquely identified by the angles ξ, χ, and ζ, see Fig. 2.
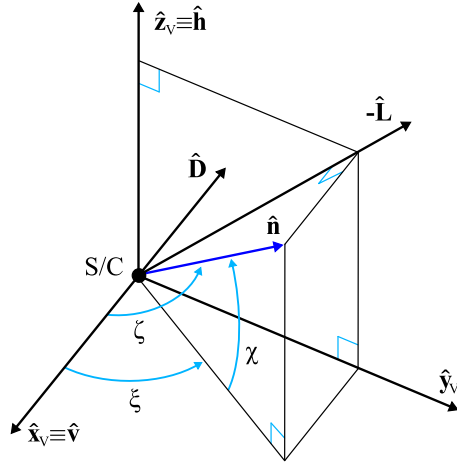
Fig. 2. Sailcraft attitude angles and aerodynamic drag, lift, and sail normal directions in the velocity reference frame, $O_V(\hat{\boldsymbol{x}}_V, \hat{\boldsymbol{y}}_V, \hat{\boldsymbol{z}}_V)$.

These variables are correlated as:

$$\cos\zeta = \cos\xi \cos\chi \tag{2}$$

The range for each of these angles depends on the instantaneous position of the Sun with respect to the sailcraft, in agreement with the assumption that the sail normal has no component pointing towards the Sun. Using these angular coordinates and Eq. (2), the sail normal direction expressed in frame O_V, $\hat{\boldsymbol{n}}_V$, is defined as:

$$\hat{\boldsymbol{n}}_V = \cos\zeta \hat{\boldsymbol{x}}_V + \cos\chi \sin\xi \hat{\boldsymbol{y}}_V + \sin\chi \hat{\boldsymbol{z}}_V \tag{3}$$

Fig. 2 also illustrates the aerodynamic drag direction, $\hat{\boldsymbol{D}}$, and lift direction, $\hat{\boldsymbol{L}}$: the former is always opposite to $\hat{\boldsymbol{v}}$, while the latter points either parallel or antiparallel to the projection of $\hat{\boldsymbol{n}}$ onto the $(\hat{\boldsymbol{x}}_V, \hat{\boldsymbol{z}}_V)$ plane, as expressed by the following relation:

$$\hat{\boldsymbol{L}} = -\operatorname{sign}(\cos\zeta) \frac{\sin\xi \cos\chi \hat{\boldsymbol{y}}_V + \sin\chi \hat{\boldsymbol{z}}_V}{\|\sin\xi \cos\chi \hat{\boldsymbol{y}}_V + \sin\chi \hat{\boldsymbol{z}}_V\|} \tag{4}$$

In Eq. (4) the minus sign guarantees that $\hat{\boldsymbol{n}}_V \cdot \hat{\boldsymbol{L}} \le 0$ (which should always hold true for a flat sail), while the "sign" function takes into account the aerodynamic symmetry of the flat sail and ensures that the lift direction corresponding to the sail normal directions $\hat{\boldsymbol{n}}$ and $-\hat{\boldsymbol{n}}$ is the same. Ultimately, it is worth noting that due to the aerodynamic symmetry, the directions $\hat{\boldsymbol{v}}$, $\hat{\boldsymbol{n}}$, $\hat{\boldsymbol{L}}$, and $\hat{\boldsymbol{D}}$ all lie in the same plane.

2.1.4. Optimization reference frame

The optimization reference frame $O_O(\hat{\boldsymbol{x}}_O, \hat{\boldsymbol{y}}_O, \hat{\boldsymbol{z}}_O)$, see Fig. 3, is centered at the center of mass of the sailcraft and defined such that its $\hat{\boldsymbol{x}}_O$-axis points in the drag direction, $\hat{\boldsymbol{D}}$, the $\hat{\boldsymbol{z}}_O$-axis points along $\hat{\boldsymbol{z}}_O = (\hat{\boldsymbol{D}} \times \hat{\boldsymbol{s}})$, and the $\hat{\boldsymbol{y}}_O$-axis completes the right-handed frame.

The angle $\eta \in [0, \pi]$ is measured from the drag direction to the direction of sunlight:

$$\eta = \cos^{-1}(\hat{\boldsymbol{D}} \cdot \hat{\boldsymbol{s}}) \tag{5}$$

Within frame O_O, the sail normal direction, $\hat{\boldsymbol{n}}_O$, can be expressed using two spherical coordinate angles: ζ and γ, see Fig. 3. Then, $\hat{\boldsymbol{n}}_O$ is defined in a similar fashion to Eq. (1) as:

$$\hat{\boldsymbol{n}}_O = \cos\zeta \hat{\boldsymbol{x}}_O + \sin\zeta \sin\gamma \hat{\boldsymbol{y}}_O + \sin\zeta \cos\gamma \hat{\boldsymbol{z}}_O \tag{6}$$

The other variables in Fig. 3 will be defined in Section 3.3.2.

2.2. Equations of motion

In this article, the solar sail is assumed to be Earth bound and its motion is determined by the SRP, aerodynamic, and gravitational accelerations. Its EoM are defined in frame O_I and take the following form:

$$\ddot{\boldsymbol{r}} + \frac{\mu_\oplus}{r^3}\boldsymbol{r} = \boldsymbol{a}_{SRP}(\boldsymbol{u}(t)) + \boldsymbol{a}_{aero}(\boldsymbol{u}(t)) + \boldsymbol{a}_{J2} \tag{7}$$

where the overhead dot notation is used to indicate differentiation with respect to time t and $\mu_\oplus = 398600.4415 \text{ km}^3/\text{s}^2$ is the Earth's gravitational parameter. The vectors $\boldsymbol{r}$ and $\boldsymbol{a}$ represent the sailcraft position and acceleration vectors in frame O_I, respectively, while $\boldsymbol{u}(t) = \hat{\boldsymbol{n}}_I(t)$ is the sailcraft control vector equal to the sail normal direction in frame O_I. The subscripts "SRP" and "aero" refer to the SRP and aerodynamic accelerations, respectively, while "J2" indicates the gravitational perturbing acceleration due to the non-spherical, oblate shape of the Earth, modeled through the J_2 spherical harmonics coefficient. These accelerations will be described in more detail in the following sections. By providing an initial time, t_0, an initial sailcraft state, $\boldsymbol{X}_0 = [\boldsymbol{r}(t_0) \ \dot{\boldsymbol{r}}(t_0)]$, and the control law $\boldsymbol{u}(t)$, Eq. (7) can be used to propagate the solar-sail state vector $\boldsymbol{X}(t)$ and find the sailcraft trajectory.

2.2.1. Solar radiation pressure acceleration

The SRP acceleration model used in this work assumes the solar sail to behave as a flat, perfectly reflecting surface. Therefore, this model is often referred to as "ideal" SRP acceleration model. Unlike other models that take into account the optical properties of the sail film material [1,25–27] or more complex sail shapes [28–31], the ideal SRP acceleration model allows for a straightforward definition of the SRP acceleration, which becomes a function of the sailcraft attitude only and can be conveniently expressed in the sail-fixed reference frame O_S as [1]:

$$\boldsymbol{a}_{SRP,S} = \nu a_c \cos^2\alpha \hat{\boldsymbol{n}}_S \tag{8}$$

where $\nu \in [0, 1]$ is the shadow factor and a_c denotes the sailcraft characteristic acceleration defined as [1]:

$$a_c = \frac{2S_\oplus}{c\sigma} \tag{9}$$

with $S_\oplus = 1367 \text{ W/m}^2$ equal to the solar flux at a distance of 1 AU from the Sun [32], $c = 299792458$ m/s representing the speed of light [32], and σ the solar-sail loading parameter, equal to the ratio of the sailcraft total mass to its sail surface area. The shadow factor ν in Eq. (8) accounts for the effect of eclipses and its value ranges from 0 (no sunlight reaches the sail) to 1 (sail completely illuminated). In this article, eclipses are modeled with a conical shadow model similar to the one presented in [33] and [34], with the only difference that penumbra is treated as umbra. This means that $\nu = 0$ not only when the sailcraft is in the Earth's umbra, but also when in penumbra, thus leading to more conservative results. The Earth radius considered for this conical shadow model is $R_\oplus = 6378.1363$ km, as per the JGM-2 geopotential model (see Section 2.2.3) [32,35].

Based on Eq. (8), the expression for the SRP acceleration in frame O_I is:

$$\boldsymbol{a}_{SRP,I} = \nu a_c \cos^2\alpha \hat{\boldsymbol{n}}_I \tag{10}$$

with

$$\hat{\boldsymbol{n}}_I = R_{S \to I} \cdot \hat{\boldsymbol{n}}_S \tag{11}$$

with $\hat{\boldsymbol{n}}_S$ defined in Eq. (1) and $R_{S \to I}$ the rotation matrix to transform vectors from the O_S frame to the O_I frame, which depends on time and the sailcraft instantaneous position.
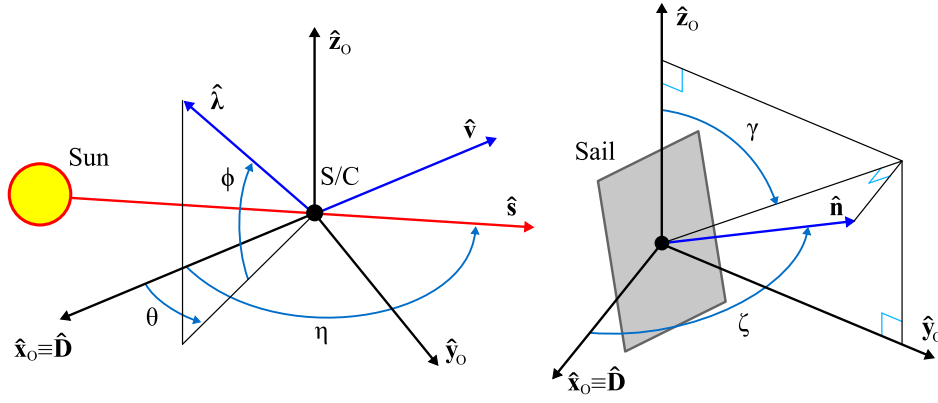
Fig. 3. Optimization reference frame, $O_O(\hat{x}_O, \hat{y}_O, \hat{z}_O)$.

2.2.2. Aerodynamic acceleration

The aerodynamic acceleration is also modeled assuming the solar sail to be a flat plate. By making the additional assumption that the sailcraft velocity is much larger than the thermal velocity of the atmospheric particles, the hyperthermal free-molecular flow model presented in [36] can be used to describe the sail aerodynamics. Such model has already been employed in [17] and [19] to analyze solar-sail trajectories in the presence of atmospheric drag and is based on the following expression for the aerodynamic acceleration in frame O_V [19]:

$$\boldsymbol{a}_{aero,V} = \boldsymbol{D} + \boldsymbol{L} = \frac{1}{2}\rho v^2 \frac{1}{\sigma}\left(C_D\hat{\boldsymbol{D}} + C_L\hat{\boldsymbol{L}}\right) \tag{12}$$

In Eq. (12), $\boldsymbol{D}$ and $\boldsymbol{L}$ represent the accelerations produced by aerodynamic drag and lift, respectively, ρ is the atmospheric density, v is the magnitude of the sailcraft inertial velocity, and C_D and C_L are the drag and lift coefficients defined as [19]:

$$C_D = 2\left[\sigma_T + \sigma_N V_R|\cos\zeta| + (2 - \sigma_N - \sigma_T)\cos^2\zeta\right]|\cos\zeta| \tag{13}$$

$$C_L = 2\left[\sigma_N V_R + (2 - \sigma_N - \sigma_T)|\cos\zeta|\right]|\cos\zeta|\sin\zeta \tag{14}$$

where σ_N and σ_T represent the normal and tangential momentum accommodation coefficients, respectively, and V_R is the ratio of the atmospheric particle average thermal velocity to the sailcraft inertial velocity. Based on [37], this article uses: $\sigma_N = \sigma_T = 0.8$, $V_R = 0.05$.

Given $\boldsymbol{a}_{aero,V}$, the expression for the aerodynamic acceleration in frame O_I becomes:

$$\boldsymbol{a}_{aero} = R_{V\rightarrow I}\cdot\boldsymbol{a}_{aero,V} \tag{15}$$

where $R_{V\rightarrow I}$ is the rotation matrix to transform vectors from the O_V frame to the O_I frame, which depends on the sailcraft instantaneous position and velocity.

2.2.2.1. Atmospheric density model

The atmospheric density ρ used in Eq. (12) is found through an averaging technique based on the NRLMSISE-00[1] model available in Matlab® [38]. As will be discussed in Section 4.1, this density averaging process is adopted to decrease the simulation runtime at the cost of a slight reduction in the accuracy of the results. The routine is as follows:

a. Given the sailcraft state at time t_0, $\boldsymbol{X}_0 = \boldsymbol{X}(t_0)$, its osculating Keplerian orbit is found.

b. A time interval $[t_0, t_0 + \Delta t]$ is considered, with $\Delta t = P/\text{SpO}$, where P is the osculating orbit's period and SpO a user-provided parameter corresponding to the number of segments per orbit to consider for the averaging.

c. Across the time interval, a set of evenly spaced time nodes $\{t_0,\ t_1,\ \ldots,\ t_{\text{NpS}-1} = t_0 + \Delta t\}$ is defined and the corresponding states along the osculating orbit $\{\boldsymbol{X}_0, \boldsymbol{X}_1,\ \ldots,\ \boldsymbol{X}_{\text{NpS}-1}\}$ are found. Note that NpS is a user-provided parameter indicating the number of nodes per orbit segment used.

d. The atmospheric density is computed through the NRLMSISE-00 model for each state of the set $\{\boldsymbol{X}_0, \boldsymbol{X}_1,\ \ldots,\ \boldsymbol{X}_{\text{NpS}-1}\}$, hence resulting in a set of densities $\{\rho_0,\ \rho_1,\ \ldots,\ \rho_{\text{NpS}-1}\}$ which are averaged to give $\overline{\rho}$.

e. The averaged value $\overline{\rho}$ is used as constant atmospheric density to numerically propagate the perturbed dynamics from $\boldsymbol{X}(t_0)$ to $\boldsymbol{X}(t_{\text{NpS}-1})$.

f. The process is repeated until the end of the simulation, taking $t_{\text{NpS}-1}$ and $\boldsymbol{X}(t_{\text{NpS}-1})$ at the end of each iteration as t_0 and $\boldsymbol{X}_0$ of the next time interval.

2.2.3. J_2 gravitational acceleration

The gravitational acceleration due to the Earth's J_2 effect in frame O_I is given by [39]:

$$\boldsymbol{a}_{J2} = -\frac{3}{2}\frac{R_\oplus^2}{r^5}J_2\mu_\oplus\left[(x_I\hat{\boldsymbol{x}}_I + y_I\hat{\boldsymbol{y}}_I)\left(1 - 5\frac{z_I^2}{r^2}\right) + z\left(3 - 5\frac{z_I^2}{r^2}\right)\hat{\boldsymbol{z}}_I\right] \tag{16}$$

where $J_2 = 1.082626925639\cdot 10^{-3}$ is the Earth's J_2 gravitational field constant of the JGM-2 geopotential model [32,35].

3. Optimal control problem

The optimal control problem considered in the present study builds on the one first investigated by McInnes in [1], where control laws to maximize the instantaneous rate of change of any given orbital element were found under unperturbed, ideal solar-sail dynamics. Hereinafter the same maximization problem will be considered, however also taking into account aerodynamic and gravitational perturbations in the equations of motion and control.

By referring to the generic orbital element as œ, the optimization problem at hand can be defined as finding the optimal control vector $\boldsymbol{u}(t) = \hat{\boldsymbol{n}}(t)$ maximizing the cost function $J(\boldsymbol{u}(t)) = \dot{\text{œ}}(\boldsymbol{u}(t))$ at any given time, subject to the dynamics described in Section 2. When the rate of change of a given orbital element is expressed through a Lagrange planetary equation, the cost function assumes the following form [1]:

$$J(\boldsymbol{u}(t)) = \dot{\text{œ}}(\boldsymbol{u}(t)) = \boldsymbol{a}(\boldsymbol{u}(t))\cdot\boldsymbol{\lambda} \tag{17}$$

where $\boldsymbol{a}$ is the sum of the accelerations on the right-hand side of Eq. (7) and $\boldsymbol{\lambda}$ is the so-called primer vector, which points along the optimal thrusting direction $\hat{\boldsymbol{\lambda}}$ that maximizes the orbital element's rate of change. It is worth noting that although the J_2 acceleration, $\boldsymbol{a}_{J2}$, influences the orbital element rate of change (and therefore the cost function $J(\boldsymbol{u})$), it does not explicitly depend on the control vector $\boldsymbol{u}$, as shown in Eq. (7). Consequently, the problem of maximizing $J(\boldsymbol{u})$ at any time is independent of the J_2 acceleration. For this reason, hereinafter only the SRP and aerodynamic accelerations are considered in the control optimization process, whereas the J_2 acceleration is taken into account only in the propagation of the EoM.

To solve the optimization problem, three different approaches are employed, depending on the relative magnitude of the SRP and aerodynamic accelerations: an SRP-based optimization, an aerodynamic-based optimization, and a full-dynamics optimization. These optimization techniques are discussed in the following sections and can be applied to find the optimal sail orientation at a specific instant in time. By applying such algorithms at each integration step during the sailcraft trajectory propagation, a sequence (history) of optimal sail normal directions representing the optimal steering law is obtained.

3.1. Solar radiation pressure-based optimization

The SRP-based optimization method is employed when the SRP acceleration is the predominant acceleration (e.g., for high-altitude orbits). In this case, the aerodynamic acceleration is considered in the propagation of the EoM but neglected in the optimization process, therefore largely simplifying the optimal control computation. Under this assumption, the optimal control history $\boldsymbol{u}^*(t)$ is found using the method devised by McInnes in [1], where an analytical formulation to compute locally optimal steering laws is presented. The method can be summarized as follows. Given the optimal thrust direction $\hat{\boldsymbol{\lambda}}$ in the O_S frame, its cone and clock angles can be defined as $\alpha_\lambda \in [0, \pi]$ and $\delta_\lambda \in [0, 2\pi]$, respectively (note that α_λ can assume values greater than $\pi/2$ as no constraint on the direction $\hat{\boldsymbol{\lambda}}$ is applied, unlike the sail normal direction $\hat{\boldsymbol{n}}$). Then, the optimal cone and clock angles of the sail normal, α^* and δ^*, are found as [10]:

$$\alpha^* = \tan^{-1}\left(\frac{-3\cos\alpha_\lambda + \sqrt{9\cos^2\alpha_\lambda + 8\sin^2\alpha_\lambda}}{4\sin\alpha_\lambda}\right) \quad (18)$$

$$\delta^* = \delta_\lambda \quad (19)$$

These optimal attitude angles maximize the SRP acceleration component along the direction $\hat{\boldsymbol{\lambda}}$, see Fig. 4. This figure displays the SRP acceleration envelope (AE) curve in the plane formed by $\hat{\boldsymbol{s}}$ and $\hat{\boldsymbol{d}}$, where $\hat{\boldsymbol{d}}$ is the projection of $\hat{\boldsymbol{n}}$ onto the $(\hat{\boldsymbol{y}}_s, \hat{\boldsymbol{z}}_s)$ plane (see Fig. 1). With α^* and δ^* given by Eqs. (18)–(19), the optimal control vector, $\boldsymbol{u}^* = \hat{\boldsymbol{n}}_I^*$, can be found using Eq. (1) and Eq. (11). It should be noted that, because of Eq. (19), the optimal sail normal direction found by the SRP-based optimization is always coplanar with $\hat{\boldsymbol{s}}$, $\hat{\boldsymbol{d}}$, and $\hat{\boldsymbol{\lambda}}$.

3.2. Aerodynamic-based optimization

The aerodynamic-based optimization method is employed when the aerodynamic acceleration is the predominant acceleration (e.g., for low-altitude orbits or when in eclipse). In this case, the SRP acceleration is considered in the propagation of the EoM but neglected in the optimization process. Similar to the method described in Section 3.1, the optimal sail attitude is found by imposing that the aerodynamic acceleration component along $\hat{\boldsymbol{\lambda}}$ is maximized. However, because of the complex expression of the
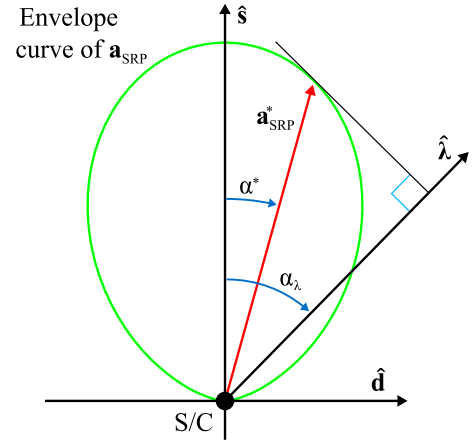
Fig. 4. Envelope curve of the SRP acceleration in the $(\hat{\boldsymbol{s}}, \hat{\boldsymbol{d}})$ plane.

aerodynamic AE surface, α^* and δ^* are found using a root-finding method. Since the aerodynamic AE surface is symmetric with respect to the $\hat{\boldsymbol{x}}_V$-axis, the intersection of this surface with a plane passing through the $\hat{\boldsymbol{x}}_V$-axis is considered, which results in an AE curve. An illustration of the aerodynamic AE curve in the $(\hat{\boldsymbol{L}}, \hat{\boldsymbol{D}})$ plane is given in Fig. 5, where the variables used to describe the optimization procedure are also shown.

By using Eq. (12), the angle ψ measured from the direction $\hat{\boldsymbol{D}}$ to the acceleration vector $\boldsymbol{a}_{aero}$ can be defined as:

$$\psi = \tan^{-1}\left(\frac{\|\boldsymbol{L}\|}{\|\boldsymbol{D}\|}\right) = \tan^{-1}\left(\frac{C_L}{C_D}\right) \quad (20)$$

As shown by Eq. (13) and (14), C_L and C_D are functions of ζ, and therefore so is ψ. Its maximum value, ψ_{max}, can then be found by imposing:

$$\frac{d\psi}{d\zeta} = 0 \Leftrightarrow \frac{d}{d\zeta}\left(\frac{C_L}{C_D}\right) = \frac{C_L' C_D - C_L C_D'}{C_D^2} = 0 \quad (21)$$

In Eq. (21), C_D' and C_L' are the derivatives of C_D and C_L with respect to ζ:

$$C_D' = -[2\sigma_N V_R + 3(2 - \sigma_N - \sigma_T)\cos\zeta]\sin 2\zeta - 2\sigma_T \sin\zeta \quad (22)$$

$$C_L' = \frac{3}{2}(2 - \sigma_N - \sigma_T)\cos 3\zeta + 2\sigma_N V_R \cos 2\zeta$$
$$+ \frac{1}{2}(2 - \sigma_N - \sigma_T)\cos\zeta \quad (23)$$

Equation (21) is solved using Matlab®'s root-finding function *fzero* with a tolerance of 10^{-10} rad.

The angle $\psi_\lambda \in [0, \pi]$ is measured from the direction $\hat{\boldsymbol{D}}$ to the direction $\hat{\boldsymbol{\lambda}}$ and based on its value two different scenarios can be defined. If $\psi_{max} < \psi_\lambda - \pi/2$, the aerodynamic acceleration vector with the largest component along $\hat{\boldsymbol{\lambda}}$ is a zero vector, i.e., the sail is oriented parallel to the wind flow with an optimal attitude angle of $\zeta^* = \pi/2$. Instead, if $\psi_{max} \geq \psi_\lambda - \pi/2$, a non-trivial solution for ζ^* exists, which can be found by imposing that the direction perpendicular to $\hat{\boldsymbol{\lambda}}$ and the tangent to the AE curve, $\hat{\boldsymbol{\tau}}$, are aligned, see Fig. 5. This condition is equivalent to:

$$\varepsilon - \left(\psi_\lambda - \frac{\pi}{2}\right) = 0 \quad (24)$$

where $\varepsilon \in [-\pi/2, \pi/2]$ is a function of ζ and is defined as the angle measured from the direction $\hat{\boldsymbol{D}}$ to the direction $\hat{\boldsymbol{\tau}}$:

$$\varepsilon = \tan^{-1}\left(\frac{C_L'}{C_D'}\right) \quad (25)$$
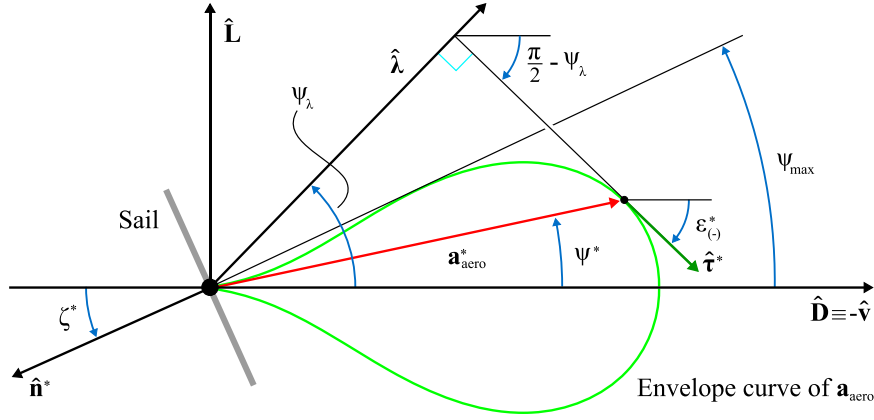
Fig. 5. Envelope curve of the aerodynamic acceleration in the $(\hat{L}, \hat{D})$ plane and variables used to find the optimal aerodynamic acceleration.

Note that ε is illustrated in Fig. 5 with the subscript "$(-)$" to indicate the direction in which this angle decreases. The non-trivial solution ζ^* can be found by solving Eq. (24) with a root-finding method (again, in the present work, Matlab®'s *fzero* function is used with a tolerance of 10^{-10} rad).

After computing the angle ζ^*, the optimal direction of the normal vector in frame O_I, $\hat{n}_I^*$, can be found by considering the aerodynamic symmetry of the problem, for which $\hat{n}$ always lies in the $(\hat{L}, \hat{D})$ plane and is coplanar with $\hat{v}$ and $\hat{\lambda}$. Given the latter two directions expressed in frame O_I, $\hat{v}_I$ and $\hat{\lambda}_I$, it is possible to compute the optimal direction $\hat{n}_I^*$ in the $(\hat{L}, \hat{D})$ plane at an angular distance ζ^* from $\hat{v}_I$ as:

$$\hat{n}_I^* = \cos(\zeta^*)\hat{v}_I + \sin(\zeta^*)\left[\frac{\hat{v}_I \times \hat{p}}{\|\hat{v}_I \times \hat{p}\|} \times \hat{v}_I\right] \qquad (26)$$

where $\hat{p} = -\hat{\lambda}_I$ if $\zeta^* \neq \pi/2$. If $\zeta^* = \pi/2$, no lift or drag is generated by the sail and any direction of $\hat{n}$ perpendicular to $\hat{v}$ is optimal. In this case, the optimal sail normal direction, $\hat{n}_I^*$, is arbitrarily chosen to be the direction with the smallest possible angle with the sailcraft inertial position unit vector, $\hat{r}$, such that $\hat{p} = \hat{r}$ in Eq. (26). The sail normal direction found through Eq. (26) does not take into account the direction of sunlight, $\hat{s}$. As such, it is possible that $\hat{n}_I^*$ has a component in the direction of the Sun, meaning that the cone angle α is not defined and the SRP acceleration cannot be computed (see Sections 2.1.2 and 2.2.1). This issue can be solved by considering the aerodynamic symmetry of the sail, for which the same aerodynamic acceleration is found for both $\hat{n}_I^*$ and $-\hat{n}_I^*$. Based on this, a final check on the direction $\hat{n}_I^*$ can be implemented. If $\hat{n}_I^* \cdot \hat{s} \geq 0$, $\hat{n}_I^*$ has no component in the direction of the Sun and therefore it can be taken as the final optimal sail normal direction. Conversely, if $\hat{n}_I^* \cdot \hat{s} < 0$, $-\hat{n}_I^*$ is taken as the optimal sail normal vector.

3.3. Full-dynamics optimization

The full-dynamics optimization technique is used when the aerodynamic and SRP accelerations are of comparable magnitudes. Similar to the procedures used in Sections 3.1 and 3.2, an AE surface is defined and the sail orientation maximizing the acceleration component along $\hat{\lambda}$ is sought. However, when considering both SRP and aerodynamics the set of all possible sail accelerations forms a highly-nonlinear envelope surface whose shape is time variant. Indeed, whereas the SRP-based and aerodynamic-based AE curves presented in Sections 3.1 and 3.2 are shape-invariant when expressed in the sunlight and velocity reference frames, respectively, the shape of the full dynamics AE surface depends on the relative orientation of the instantaneous $\hat{s}$ and $\hat{v}$ directions, as well as the

relative magnitude of the SRP characteristic acceleration, a_c, compared to the maximum aerodynamic acceleration, $a_{aero,max}$. In addition, the envelope surface can also be self-intersecting, meaning that different sail attitudes can result in the same total acceleration vector. An example of such a surface is given for $\hat{s} \perp \hat{v}$ and $a_c = a_{aero,max}$ in Fig. 6, where the corresponding SRP and aerodynamic AE surfaces are also shown for comparison. Because of the complex, time-variant shape of the AE surface and the fact that, to the best of the authors' knowledge, no analytical solution to the optimization problem exists, a numerical approach is proposed in the subsequent subsections.

3.3.1. Numerical approaches to the optimization problem

The most straightforward way of solving the full-dynamics optimization problem, is through a grid search approach. This translates into taking a large set of attitude angles, evaluating the corresponding acceleration vectors, a_{SRP} and a_{aero}, using these accelerations to determine the AE surface, and eventually retrieving the orientation that maximizes the acceleration component along the $\hat{\lambda}$ direction. However, since the shape of the AE surface depends on the instantaneous sailcraft state and time, this routine ought to be performed at each propagation time step. As a consequence, although such a technique works in theory and ensures that the global optimal solution is found, in practice a large number of function evaluations is required even for small propagation times, thereby yielding impractical runtimes.

Alternatively, techniques such as the interior-point optimization method (e.g., available in Matlab®'s function *fmincon*) can be applied. Although this optimization technique requires less computational effort than the grid search, it requires an initial guess for the optimal sail orientation. For the first propagation time step such an initial guess can be found by using a grid search, whereas for the subsequent time steps the initial guess can be provided by the optimal attitude found in the previous time step. However, the attitudes found are often sub-optimal because it is only a local optimization method. Indeed, the shape of the AE surface can become highly nonlinear during the propagation, which translates into multiple local optima of the cost function $J(u)$. In addition, for some steering laws, the primer direction, $\hat{\lambda}$, can change in a discontinuous manner between adjacent propagation time steps. When using the optimal attitude found in the previous propagation step as initial guess for the current step, this can cause the optimizer to get trapped in a local minimum.

To circumvent the downsides of the techniques mentioned above, this article proposes a new optimization approach, whose main advantages are a short runtime for the trajectory propagation and the global validity of the optimal solutions found. The basic idea behind the proposed approach is to first find the global
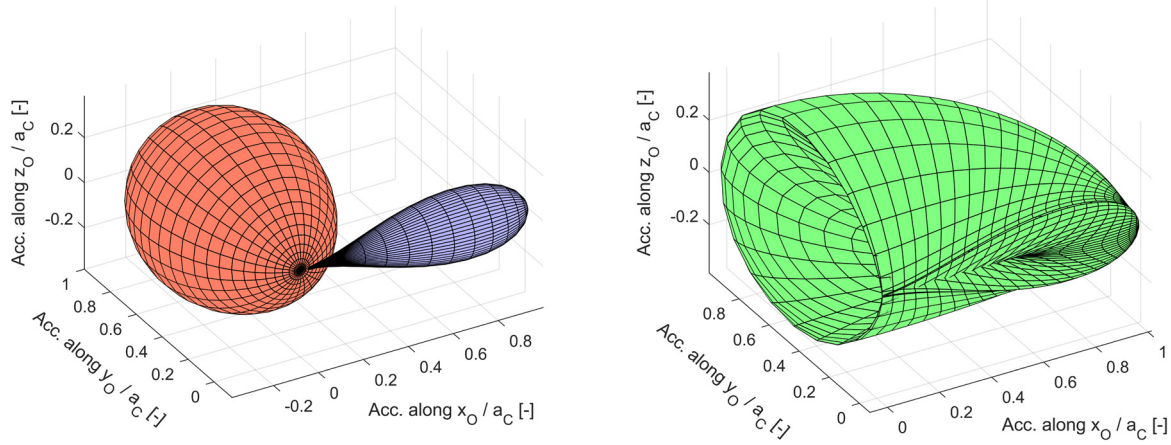
Fig. 6. SRP AE surface (left, red), aerodynamic AE surface (left, blue), and full dynamics AE surface (right) in frame O_O, for $a_c = a_{aero,max}$ and $\hat{s} = \hat{y}_O$ (corresponding to $\eta = \pi/2$). (For interpretation of the colors in the figure(s), the reader is referred to the web version of this article.)

optimal solution of the cost function $J(\boldsymbol{u})$ for a large variety of scenarios and subsequently interpolate these pre-computed optimal solutions at each time step in the trajectory propagation to retrieve an interpolated global optimum. In this way, the attitude optimization computation is completely separated from the trajectory propagation, thereby allowing the latter to be performed with small computational effort. Hereinafter this optimization method is referred to as the "Pre-run Optimization and in-run INTerpolation" (POINT) method. The two phases of the method, the optimization and interpolation phases, are described in detail in Sections 3.3.2 and 3.3.3.

3.3.2. Pre-run optimization phase

The pre-run optimization phase of the POINT method aims to solve the optimization problem for a large set of different scenarios, i.e., for a large variety of combinations of AE shapes and $\hat{\boldsymbol{\lambda}}$ directions. To do so, the optimization problem is parametrized by four parameters: R, η, θ, and ϕ.

- The coefficient R represents the ratio of the maximum SRP acceleration to the maximum aerodynamic acceleration and its value affects the AE shape. This coefficient indicates to what extent the AE shape is similar to the AE shape of the pure SRP acceleration or pure aerodynamic acceleration. For example, for increasing values of R, the SRP acceleration increasingly dominates the aerodynamic acceleration, meaning that the AE shape becomes more similar to the SRP one. On the other hand, for R values close to zero, the aerodynamic acceleration is dominant so that the AE shape tends to resemble the AE shape of the pure aerodynamic case. By taking into account that the maximum SRP acceleration is equal to the solar-sail characteristic acceleration and that the maximum aerodynamic acceleration is achieved for $\zeta = 0$ (i.e., when the sail is perpendicular to the wind flow), R can be expressed using Eq. (9), (12), (13), and (14) as:

$$R = \frac{a_c}{a_{aero,max}} = \frac{S_\oplus}{c} \frac{2}{\rho v^2} \frac{1}{[2 - \sigma_N(1 - V_R)]} \quad (27)$$

Since both the SRP and aerodynamic accelerations are inversely proportional to the sail loading parameter σ, R is independent of σ. This result implies that the AE shape – and thus the entire optimization process - is independent of the sail loading parameter.

- The parameter η determines the relative orientation of the SRP and aerodynamic AE surfaces and its definition is given in Sec-

tion 2.1.4. Together with R, it uniquely defines the AE shape of the full-dynamics case, which results from combining the two separate (i.e., pure SRP and pure aerodynamic) AE surfaces. An example is given in Fig. 6, where the combination of the AE surfaces in the left plot generates the one in the right plot.

- The angles θ and ϕ represent the spherical coordinates of the $\hat{\boldsymbol{\lambda}}$ direction in the O_O frame (see Fig. 3).

Each set $\{R, \eta, \theta, \phi\}$ represents a specific optimization problem which can be solved numerically to find the corresponding optimal sail attitude. To achieve this, a grid search is performed over the angles ζ and γ of the sail normal direction in frame O_O (see Fig. 3). To explore the entire parameter space, a four-dimensional grid of discrete values for R, η, θ, and ϕ is created across the following domains: $R \in [R_{min}, R_{max}]$, $\eta \in [0, \pi]$, $\theta \in [0, 2\pi]$, and $\phi \in [0, \pi/2]$. R_{min} and R_{max} are two threshold parameters whose values are defined in Section 4.4 and determine when the full-dynamics optimization should be used instead of the aerodynamic-based optimization ($R < R_{min}$) or the SRP-based optimization ($R > R_{max}$). Also, it is worth noting that only positive values of ϕ are considered because of the symmetry of the AE surface with respect to the $(\hat{\boldsymbol{x}}_O, \hat{\boldsymbol{y}}_O)$ plane. Due to this symmetry, each pair of angles $\pm\phi$ corresponds to optimal normal directions in the O_O frame, $\hat{\boldsymbol{n}}_O^*$, that differ only in the sign of the component along the $\hat{\boldsymbol{z}}_O$ direction, i.e., $\hat{\boldsymbol{n}}_O^* = \left[n_{O,x}^*, n_{O,y}^*, \pm n_{O,z}^*\right]^T$. Therefore, whenever a $\hat{\boldsymbol{\lambda}}$ direction with $\phi < 0$ is encountered during the trajectory propagation, the optimal normal direction $\hat{\boldsymbol{n}}_O^*$ computed for $-\phi$ (>0) in the pre-run optimization phase is retrieved and the sign of its $n_{O,z}^*$-component is changed to obtain the optimal attitude for $\phi < 0$.

The computation of the four-dimensional, pre-optimized grid can require a significant computational effort, particularly because of the large domains for the parameters R, η, θ, and ϕ. One way to overcome this issue is to analyze the problem at hand and determine in advance the range of $\hat{\boldsymbol{\lambda}}$ directions achievable along the trajectory. In this way, the θ and ϕ domains can be shrunk and the number of discrete points to consider in the grid can be reduced, hence lowering the computational effort. This procedure has been used to create all pre-optimized grids of Sections 4 and 5. Indeed, in these sections the orbit raising and inclination increase steering laws are discussed, for which the $\hat{\boldsymbol{\lambda}}$ direction always points opposite and perpendicular to $\hat{\boldsymbol{x}}_O$, respectively.

3.3.3. In-run interpolation phase

To describe the interpolation process adopted in the POINT method, each set of variables $\{R, \eta, \theta, \phi\}$ will be represented as a point $\boldsymbol{S} = [S_1, S_2, S_3, S_4]^T = [R, \eta, \theta, \phi]^T$ in a four-dimensional vector space. In this way, each grid point computed in the pre-run optimization phase is represented by $\boldsymbol{S} \in \mathbb{R}^{4\times1}$, while the set of all grid points is $\Sigma = \{\boldsymbol{S}_1, \boldsymbol{S}_2, \ldots, \boldsymbol{S}_N\} \in \mathbb{R}^{4\times N}$, with N equal to the total number of grid points.

At each time step of the trajectory propagation, specific values for R, η, θ, and ϕ are encountered which identify a target point $\boldsymbol{S}_t = [S_{t,1}, S_{t,2}, S_{t,3}, S_{t,4}]^T$. In general, $\boldsymbol{S}_t$ will be different from any of the points $\boldsymbol{S}$ available in Σ. However, it is always possible to find a subset of neighboring points $\Sigma_{NBH} \subset \Sigma$ close to $\boldsymbol{S}_t$ that encloses the region of space where $\boldsymbol{S}_t$ is located. This region is obtained by considering, for each component $S_{t,k}$, the two closest neighboring values in the pre-optimized grid, $S_{t,k}^-$ and $S_{t,k}^+$, such that $S_{t,k} \in [S_{t,k}^-, S_{t,k}^+]$, with $k = 1, \ldots, 4$. This results in $2^4 = 16$ possible combinations representing the coordinates of the points in $\Sigma_{NBH} \in \mathbb{R}^{4\times16}$, i.e.:

$$\Sigma_{NBH} = \begin{cases} \boldsymbol{S}_{NBH,1} = \left[S_{t,1}^-, S_{t,2}^-, S_{t,3}^-, S_{t,4}^-\right]^T \\ \boldsymbol{S}_{NBH,2} = \left[S_{t,1}^-, S_{t,2}^-, S_{t,3}^-, S_{t,4}^+\right]^T \\ \boldsymbol{S}_{NBH,3} = \left[S_{t,1}^-, S_{t,2}^-, S_{t,3}^+, S_{t,4}^-\right]^T \\ \boldsymbol{S}_{NBH,4} = \left[S_{t,1}^-, S_{t,2}^-, S_{t,3}^+, S_{t,4}^+\right]^T \\ \boldsymbol{S}_{NBH,5} = \left[S_{t,1}^-, S_{t,2}^+, S_{t,3}^-, S_{t,4}^-\right]^T \\ \boldsymbol{S}_{NBH,6} = \left[S_{t,1}^-, S_{t,2}^+, S_{t,3}^-, S_{t,4}^+\right]^T \\ \vdots \\ \boldsymbol{S}_{NBH,16} = \left[S_{t,1}^+, S_{t,2}^+, S_{t,3}^+, S_{t,4}^+\right]^T \end{cases} \tag{28}$$

Since each point in Σ_{NBH} corresponds to an optimal sail orientation computed in the pre-run optimization phase, a set $\Gamma_{NBH} \in \mathbb{R}^{3\times16}$ of 16 optimal normal directions in frame O_O, $\hat{\boldsymbol{n}}_O^*$, is also given. The interpolation of these normal directions is performed through a normalized inverse distance weighted (IDW) technique [40] and applied to the problem at hand as follows. Before the interpolation is performed, $\boldsymbol{S}_t$ and the points in Σ_{NBH} are normalized[2] to restrict the domain of their four components to $[0, 1]$, thus resulting in the normalized target point $\overline{\boldsymbol{S}}_t$ and neighboring set $\overline{\Sigma}_{NBH} = \{\overline{\boldsymbol{S}}_{NBH,1}, \ldots, \overline{\boldsymbol{S}}_{NBH,16}\}$. From these, the vector $\boldsymbol{\varrho} = [\varrho_1, \ldots, \varrho_{16}]^T$ is computed which contains the inverses of the Euclidean distances between $\overline{\boldsymbol{S}}_t$ and $\overline{\boldsymbol{S}}_{NBH,1}, \ldots, \overline{\boldsymbol{S}}_{NBH,16}$. The inverse distance weight vector, $\boldsymbol{w} \in \mathbb{R}^{16\times1}$, is also calculated as:

$$\boldsymbol{w} = [w_1, \ldots, w_{16}]^T = \frac{\boldsymbol{\varrho} \circ \boldsymbol{\varrho}}{\boldsymbol{\varrho}^T \cdot \boldsymbol{\varrho}} \tag{29}$$

where $\circ$ indicates the element-wise Hadamard product of two vectors [41]. Finally, the optimal normal directions in Γ_{NBH}, i.e., $\hat{\boldsymbol{n}}_{O,NBH,1}^*, \ldots, \hat{\boldsymbol{n}}_{O,NBH,16}^*$, are used to define the following matrix $\mathcal{N} \in \mathbb{R}^{3\times16}$:

$$\mathcal{N} = \left[\hat{\boldsymbol{n}}_{O,NBH,1}^*, \ldots, \hat{\boldsymbol{n}}_{O,NBH,16}^*\right] \tag{30}$$

which is then used to find the final interpolated normal direction, $\hat{\boldsymbol{n}}_O^*$, as:

$$\hat{\boldsymbol{n}}_O^* = \frac{\mathcal{N} \cdot \boldsymbol{w}}{\|\mathcal{N} \cdot \boldsymbol{w}\|} \tag{31}$$

3.3.3.1. Handling of local optima

As the neighboring points $\boldsymbol{S}_{NBH,1}, \ldots, \boldsymbol{S}_{NBH,16}$ consider different values for R, η, θ, and ϕ, they represent optimization problems with slightly different AE shapes and $\hat{\boldsymbol{\lambda}}$ directions. However, due to the high nonlinearity of the problem, in certain cases slightly different AE shapes and primer vector's directions make the optimal normal directions $\hat{\boldsymbol{n}}_{O,NBH,1}^*, \ldots, \hat{\boldsymbol{n}}_{O,NBH,16}^*$ differ substantially. Such scenarios take place when the target point considered, $\boldsymbol{S}_t$, corresponds to an optimization problem with regions of similar degrees of local optimality. These regions contain both the globally optimal solution and other locally optimal solutions. Although all these optimal solutions are associated to similar cost function values, in some cases the corresponding sail normal directions can significantly differ from one another. When this kind of optimization problem is encountered, small variations in the components of $\boldsymbol{S}_t$ yield slight variations in the cost function values of these optimal regions. This in turn can make the global optimum shift from one region to another and the corresponding optimal normal direction suddenly change. For this reason, when dealing with this kind of optimization problems, the optimal normal directions found for the neighboring points $\boldsymbol{S}_{NBH,1}, \ldots, \boldsymbol{S}_{NBH,16}$ strongly differ from each other and, as a consequence, using IDW interpolation yields an interpolated solution $\hat{\boldsymbol{n}}_O^*$ that is less optimal than $\hat{\boldsymbol{n}}_{O,NBH,1}^*, \ldots, \hat{\boldsymbol{n}}_{O,NBH,16}^*$.

To avoid this issue, the POINT method makes use of an algorithm that aims to identify such locally optimal regions before the interpolation. In this way, it is possible to consider each region separately in the interpolation phase and compute different optimal solutions $\hat{\boldsymbol{n}}_O^*$, which contain the global optimum. The algorithm is based on the idea that different locally optimal regions of the solution space correspond to locally optimal sail normal vectors pointing in different directions. The angular distances between the optimal normal directions of Γ_{NBH} allow to define clusters of normal directions, which in turn identify the local optimal regions. In this article the cluster detection has been performed by means of a hierarchical clustering algorithm with single-linkage criterion [42]. The algorithm computes the norm of the difference of each pair of normal directions in Γ_{NBH}, compares these norms with a threshold value, and determines the number of clusters in Γ_{NBH}. More specifically, in this article the Matlab® function *cluster* is employed using a distance-based criterion and a hierarchical cluster tree (defined through the function *linkage*) built with a "shortest Euclidean distance" method. The value used for the threshold is $2\sin(\pi/60)$, corresponding to a minimum angle of 6 deg between normal directions of different clusters. This value is tuned based on the knowledge of the optimization problem under investigation, the number of grid points in Σ, and some trial and error. When the optimization problem is not characterized by multiple locally optimal regions, the algorithm returns one unique cluster that coincides with Γ_{NBH} and therefore the interpolation routine can be performed as explained in the previous section. Conversely, if different clusters are found, for each cluster in Γ_{NBH} the corresponding points in Σ_{NBH} are taken and the normalization and interpolation routines are performed separately on each subset of Σ_{NBH} to find multiple locally optimal solutions $\hat{\boldsymbol{n}}_O^*$. From these, the normal direction corresponding to the largest cost function value is taken as the global optimal solution.

4. Validation and testing

In this section, different analyses are presented that aim to tune all parameters regulating the atmospheric density averaging algorithm and the POINT optimization method. In Table 1 the simulation settings are given for each of the four tests presented in sections 4.1 to 4.4.

---

[2] When performing the normalization, two of the three Cartesian components of the $\hat{\boldsymbol{\lambda}}$ direction are considered instead of the spherical coordinates θ and ϕ to avoid dealing with discontinuous variables in the interpolation process.

Table 1

Simulation settings used for the validation and testing in Section 4.

Parameter	Test/Section			
	4.1	4.2	4.3	4.4
Sim. start	July 1st, 2022			
Sim. duration	10 days	1 orbital period		
a_c	0.05 mm/s^2			
Initial state	ACS3, with variations in a and i	ACS3		
Integrator	MATLAB®'s *ode45*			
Rel./Abs. tol.	10^{-12}	10^{-8}		
Dynamics	Earth's Central Gravity + SRP + Aerodynamics			
Atmospheric model	Avg. NRLMSISE-00 model (SpO: $2 \div 200$, NpS: $2 \div 20$)	Avg. NRLMSISE-00 model (SpO: 25, NpS: 4)		Constant ρ
Reference solution	Full NRLMSISE-00 model + SRP-based optimal control	Avg. NRLMSISE-00 model (SpO: 25, NpS: 4) + Full-dynamics, grid search-based optimal control with $\Delta\alpha = \Delta\delta = 0.01$ deg		Constant ρ + SRP-based or aerodynamic-based control
Control optimization algorithm	SRP-based	Full-dynamics		Full-dynamics
Steering Law	a	a and i		
$\Delta\Lambda$	(none)	1 deg	$0.1 \div 2$ deg	1 deg
ΔR	(none)	1.21	$1.1^{1/4} \div 1.1^4$	1.21
$\Delta\gamma$	(none)	$\Delta\Lambda/10$		
$\Delta\zeta$	(none)			

All analyses make use of the ACS3 mission as baseline scenario, corresponding to a solar-sail characteristic acceleration of $a_c = 0.05$ mm/s^2, a simulation start time of July 1st, 2022 (i.e., the expected deployment date of the solar sail), and the following vector of initial Keplerian elements:

$$[a_0, e_0, i_0, \Omega_0, \omega_0, \vartheta_0]^T$$
$$= [7093.1363 \text{ km}, 0, 98.2489 \text{ deg}, 10.5029 \text{ deg}, 0 \text{ deg}, 0 \text{ deg}]^T$$
(32)

where a is the semi-major axis (SMA), e the eccentricity, i the inclination, Ω the right ascension of the ascending node, ω the argument of perigee, ϑ the true anomaly, and the subscript "0" denotes the initial value of these variables[3]. Note that these Keplerian elements represent a circular, Sun-synchronous orbit with altitude $h_0 = a_0 - R_\oplus = 715$ km and local time of the ascending node (LTAN) at 6AM (corresponding to a dawn-dusk orbit). As shown in Table 1, the dynamical model used in all tests considers the Earth's central gravitational acceleration, SRP acceleration, and aerodynamic acceleration. On the other hand, the J_2 gravitational acceleration is not considered. This choice is justified by the fact that the parameter tuning is conducted on test cases that consider an increase in SMA or inclination. The J_2 perturbation has no secular effect on these Keplerian elements, only a short-term periodic effect [32]. Therefore, including the J_2 acceleration would only add significant noise to the results. Propagations are performed using MATLAB®'s *ode45* integrator for all tests, with absolute and relative tolerances of 10^{-8} or 10^{-12} depending on the simulation duration.

4.1. Tuning of the atmospheric density model

The parameters affecting the density averaging procedure described in Section 2.2.2.1 are the number of averaging segments per orbit, SpO, and the number of nodes per orbit segment, NpS. By tuning these parameters, a significant reduction in runtime can be achieved at the cost of a decreased accuracy in the results. These two criteria (runtime and accuracy) form the basis of the trade-off described hereinafter.

As shown in Table 1, the steering law adopted is an orbit raising steering law computed using the SRP-based optimization of Section 3.1, meaning that aerodynamic drag is not considered in the optimization but only in the propagation of the dynamics. The choice for this steering law is based on the fact that aerodynamic drag negatively affects the rate of change of the orbital altitude, enlarging the effect of different averaged density models when aerodynamic drag is not accounted for in the optimization process. The achieved increase in altitude is taken as a metric for the accuracy. More specifically, the relative error, $\epsilon_{\Delta a,rel}$, defined as

$$\epsilon_{\Delta a,rel} = \left| \frac{\Delta a - \Delta a_{ref}}{\Delta a_{ref}} \right|$$
(33)

is used, where Δa and Δa_{ref} are the increases in SMA achieved with the averaged density model and the full NRLMSISE-00 model, respectively. Similarly, the relative runtime, ΔT_{rel}, is used as a measure of the runtime reduction obtained by using a specific averaged atmospheric density model:

$$\Delta T_{rel} = \left| \frac{\Delta T}{\Delta T_{ref}} \right|$$
(34)

where ΔT and ΔT_{ref} are the runtimes required by the averaged density model and the full NRLMSISE-00 model for the entire propagation, respectively. In the analyses, the sailcraft characteristics, simulation start time, and orbital parameters correspond to

---

[3] ACS3 mission data taken from personal communication with W.K. Wilkie, Principal Investigator of the ACS3 mission, NASA Langley Research Center, September 2021.
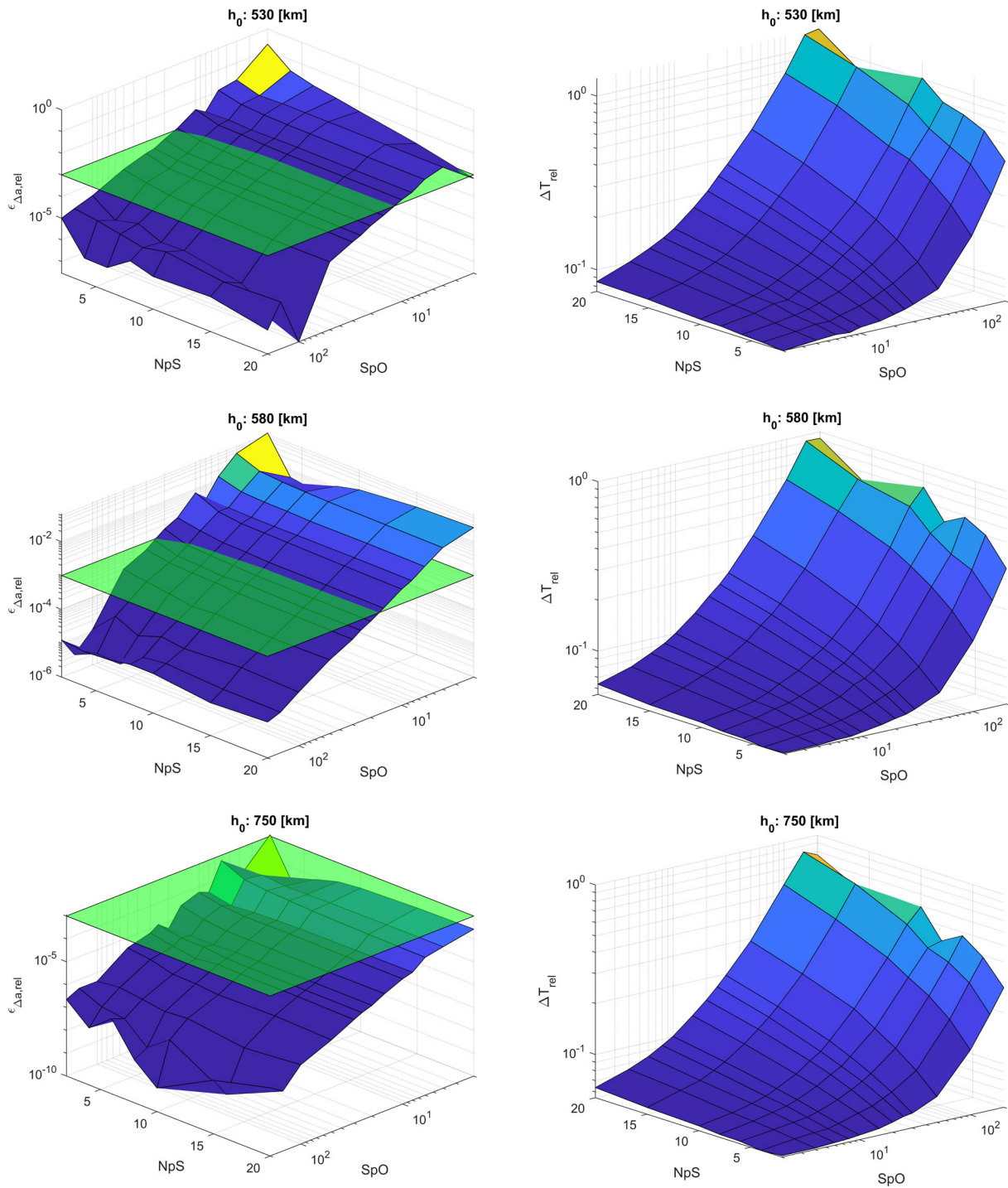
Fig. 7. $\epsilon_{\Delta a,rel}$ and ΔT_{rel} as function of the initial altitude, SpO, and NpS.

those of the ACS3 mission except for the initial orbital altitude and inclination. Indeed, the metrics $\epsilon_{\Delta a,rel}$ and ΔT_{rel} are computed for three different initial altitudes to account for the effect of different ranges of acceleration ratios R on the results. In particular, the altitudes considered are 530 km, 580 km, and 750 km, corresponding to $R \in [1/23.9797, 1.1656]$ (aerodynamic-dominated case), $R \in [1/3.2528, 2.4394]$ (intermediate case), and $R \in [2.7672, 39.7815]$ (SRP-dominated case), respectively. Also, the initial altitudes of 530 km, 580 km, and 750 km correspond to Sun-synchronous inclinations of 97.5158, 97.7090, and 98.3933 deg, respectively.

The resulting values for $\epsilon_{\Delta a,rel}$ and ΔT_{rel} for each initial altitude, SpO, and NpS are displayed in Fig. 7. The SpO values used

to generate the surface plots are {2, 4, 6, 8, 10, 15, 20, 25, 30, 50, 100, 150, 200}, while the NpS values considered are {2, 4, 6, 8, 10, 15, 20}. The plots on the left-hand side of Fig. 7 also show a plane corresponding to $\epsilon_{\Delta a,rel} = 10^{-3}$. This value is chosen as the maximum allowable value for $\epsilon_{\Delta a,rel}$ in the trade-off between different combinations of SpO and NpS. Fig. 7 shows that – for any given altitude – decreasing values of SpO and NpS yield smaller runtimes at the cost of larger relative errors. However, while the value for NpS affects the runtime to some extent, no clear correlation can be determined between NpS and the relative error. Based on this, a final value of NpS = 4 is chosen for all altitudes and will be considered in the following analysis to determine the value for SpO.

Unlike NpS, the value for SpO largely affects both $\epsilon_{\Delta a,rel}$ and ΔT_{rel} and the extent of the effect depends on the initial altitude:

- $h_0 = 530$ km: In order to achieve the shortest possible runtime while keeping the relative error below the threshold, $\epsilon_{\Delta a,rel} < 10^{-3}$, a value for SpO ≥ 20 should be selected.
- $h_0 = 580$ km: By the same logic, SpO ≥ 25 in order for the relative error constraint to be met.
- $h_0 = 750$ km: In this case, the relative error is considerably below the threshold for any SpO.

Based on the above considerations, a final value of SpO $= 25$ is used for all altitude regimes, corresponding to $\epsilon_{\Delta a,rel}$ in the range $[7.17026 \cdot 10^{-6},\ 5.83754 \cdot 10^{-4}]$ and ΔT_{rel} in the range $[7.76874 \cdot 10^{-2},\ 1.07546 \cdot 10^{-1}]$.

4.2. Validation of the full-dynamics POINT optimization

In this section, two cases are discussed which aim to validate the POINT optimization method and show its accuracy, both for an orbit raising steering law and an inclination increase steering law. This is achieved by propagating one single orbit, optimizing its control with the POINT method, and comparing the control profile achieved with a reference solution. Based on the results of Section 4.1, the reference solution in this section uses the averaged NRLMSISE-00 atmospheric density model, with SpO $= 25$ and NpS $= 4$. The reference solutions for both steering laws are found by performing a grid search at each propagation time step (as explained in Section 3.3.1), with steps equal to $\Delta \alpha = \Delta \delta = 0.01$ deg for the cone and clock angles. Based on the tuning of the pre-run optimization grid that will be discussed in Section 4.3, the grid Σ used by the POINT method is defined by using an angular step, $\Delta\Lambda$, of 1 deg for the variables η, θ, and ϕ and a step of $\Delta R = 1.1^2 = 1.21$ for the acceleration ratio (see Section 4.3 for more details on the definition of ΔR). Finally, the grid search of the pre-run optimization phase of POINT is performed using $\Delta\gamma = \Delta\zeta = \Delta\Lambda/10 = 0.1$ deg as angular steps.

4.2.1. Orbit raising

For the orbit raising steering law, the control profiles of the reference solution and the POINT solution are given in Fig. 8. As can be appreciated from the zoomed-in plots of the cone and clock angle profiles, the POINT solution (in red) accurately approximates the reference solution (in blue, dashed). Also, from Fig. 8 it can be noted that the cone-angle profile exhibits instantaneous jumps, both in the reference and POINT solutions. This is due to the averaging procedure of the atmospheric density model employed, which yields a step-wise variation in the density along the orbit and, therefore, also in the acceleration ratio. This in turn affects the control computation procedure, leading to the sudden variations in α shown in the figure. As a measure of the error in optimal sail normal direction as computed by the POINT method, the angular displacement, ϵ_n, between the sail normal direction of the POINT method and the reference solution is computed at each time step. The result is displayed in Fig. 9, where the red dashed line indicates the root mean square (RMS) of ϵ_n, equal to 0.1742 deg. It should be noted that the RMS of ϵ_n depends on the angular steps $\Delta\Lambda$, $\Delta\gamma$, and $\Delta\zeta$ used in the pre-run optimization phase of POINT and are of comparable magnitudes, as one would expect when performing an interpolation. The relative error of the SMA increase, $\epsilon_{\Delta a,rel}$, is displayed in Fig. 10. This error is defined as per Eq. (33), with Δa and Δa_{ref} the increases in SMA of the POINT and reference solutions, respectively. After a sudden increase in $\epsilon_{\Delta a,rel}$ at the beginning of the simulation – which coincides with a large value for ϵ_n – the relative error stabilizes with a final value after

one orbit of $\epsilon_{\Delta a,rel} = 2.7537 \cdot 10^{-5}$. This value is deemed acceptable, also in relation to the relative error threshold of 10^{-3} used for the atmospheric density model tuning of Section 4.1.

4.2.2. Inclination increase

The α and δ angle profiles for the inclination steering laws of the POINT and reference solutions are given in Fig. 11. Here, it can be noted that the POINT solution closely resembles the reference solution. Nonetheless, the POINT solution manages to approximate the reference solution better during the first and last quarter of the orbit than in the middle part of the orbital revolution. This becomes even clearer in the zoomed-in plots of Fig. 11, as well as in Fig. 12, which displays the evolution of ϵ_n. In particular, the latter figure shows that the POINT method experiences difficulties in finding the true optimal solution in the middle part of the orbital revolution, leading to displacements in the sail normal direction in the order of some degrees. Consequently, a steep growth in the inclination-increase relative error, $\epsilon_{\Delta i,rel}$, is also observed during this time, see Fig. 13. Note that this relative error is defined similar to $\epsilon_{\Delta a,rel}$ as:

$$\epsilon_{\Delta i,rel} = \left| \frac{\Delta i - \Delta i_{ref}}{\Delta i_{ref}} \right| \tag{35}$$

where Δi_{ref} and Δi are the increases in inclination of the reference and POINT solutions, respectively. The errors observed are due to the intrinsic difficulty in increasing the inclination in the middle part of the orbit where every non-zero, out-of-plane solar-sail acceleration points opposite to $\hat{\lambda}$ and would therefore yield a negative Δi. Consequently, the optimal attitude is the one that minimizes the out-of-plane acceleration, resulting in no change in inclination, see Fig. 14. However, multiple sail attitudes lead to a Δi close to zero, hence making the search for the global optimal attitude hard for the POINT method. Despite the errors introduced in this middle part of the orbit, the relative error achieved at the end of the propagation is $\epsilon_{\Delta i,rel} = 8.4872 \cdot 10^{-6}$, which, again, is deemed acceptable in relation to the threshold of 10^{-3} used for the atmospheric density model tuning of Section 4.1.

4.3. Tuning of the pre-run optimization grid

As described in Section 3.3.3, the in-run interpolation phase of the POINT method aims to compute the interpolated optimal sail normal directions based on the grid points $S \in \Sigma$ of the pre-run optimization phase. The way in which these points are chosen and – in particular – the spacing between them, affects the accuracy of the results obtained by the interpolation. In this section, the results for different grids Σ are evaluated to determine the correlation between the accuracy of the optimal solutions found and the spacing of the grid points. Based on this, a final grid Σ is chosen.

Because this article only considers steering laws for orbit raising and inclination increase, the grid points' spacing will be evaluated separately for these two steering laws. Since the spacing of the points $S \in \Sigma$ is determined by the step used for each of the points' components (i.e., ΔR, $\Delta\eta$, $\Delta\theta$, and $\Delta\phi$), a computationally demanding, four-dimensional parametric analysis ought to be performed. To reduce the dimensionality of the parametric analysis, the angular steps of the variables η, θ, and ϕ are set equal to a common value $\Delta\Lambda$, so that $\Delta\Lambda = \Delta\eta = \Delta\theta = \Delta\phi$. The set of values used for $\Delta\Lambda$ in the parametric analysis is $\{0.1, 0.2, 0.5, 1.0, 2.0\}$ [deg], while the set for ΔR is $\{1.1^{1/4}, 1.1^{1/2}, 1.1, 1.1^2, 1.1^4\}$. It should be noted that, while $\Delta\Lambda$ represents the difference between adjacent angular values of the grid, ΔR represents the *ratio* of consecutive R values. This means that given a value R_k of the grid, the adjacent one, R_{k+1},
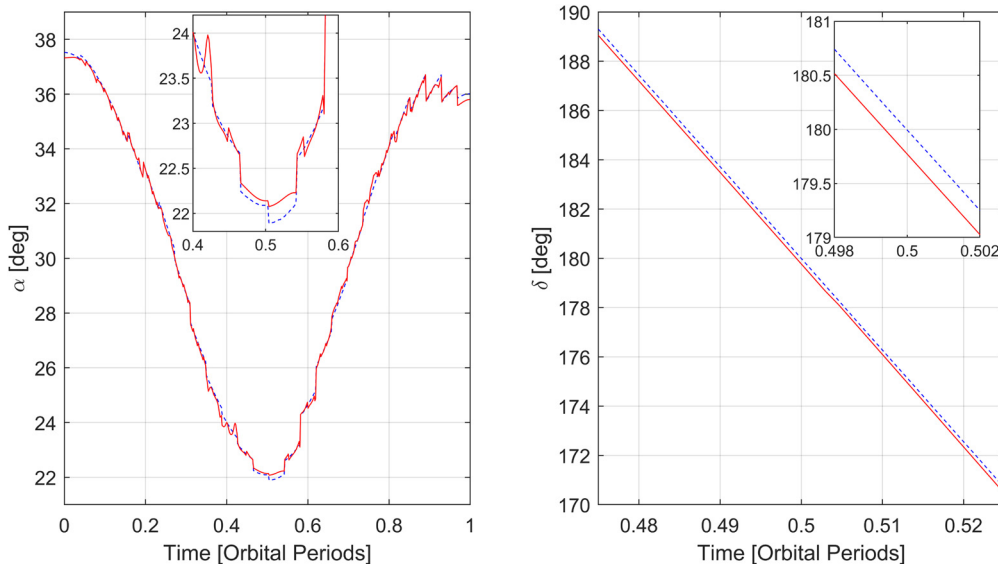
Fig. 8. Orbit raising: control profile of the reference solution (blue, dashed) and POINT solution (red, solid) over one orbital period.
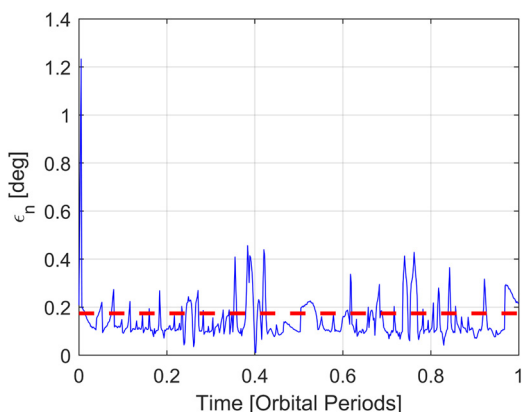
Fig. 9. Orbit raising: angular error between the sail normal directions of the reference solution and those found by the POINT method (blue, solid) and RMS of the angular error over one orbital period (red, dashed).
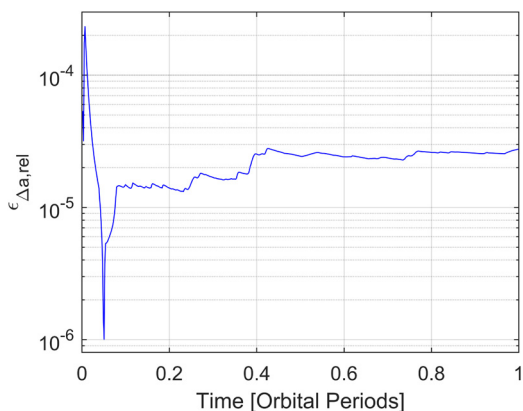
Fig. 10. Orbit raising: relative error in Δa between the reference solution and POINT solution.

is found as $R_{k+1} = R_k \cdot \Delta R$. This approach is employed because the change in shape of the AE surface with R is exponential.

To determine the correlation between the accuracy of the optimal solutions and the spacing of the grid points, the POINT optimization is run with different grids Σ and the final increases in altitude or inclination are computed and compared with a ref-

Table 2
Relative errors on Δa for each pair of $\Delta \Lambda$ and ΔR.

$\epsilon_{\Delta a,rel} \cdot 10^{-5}$		ΔR				
		$1.1^{1/4}$	$1.1^{1/2}$	1.1	1.1^2	1.1^4
$\Delta \Lambda$ [deg]	0.1	7.3042	4.9774	3.1956	7.0016	8.2448
	0.2	6.0737	4.1505	2.2168	5.5576	7.9439
	0.5	2.4879	1.8414	1.1708	2.4118	6.6047
	1.0	2.4806	1.8681	2.4475	2.7537	6.4701
	2.0	6.7333	5.4641	4.5604	6.3204	9.7635

erence optimal solution (the same reference solution as used in Section 4.2, see Table 1). The differences in final altitude/inclination are a measure of the errors introduced by using different grids Σ (i.e., different combinations of steps $\Delta \Lambda$ and ΔR).

The parametric analyses are performed using the settings presented in Table 1. In particular, the same settings as in Section 4.2 are used, with the only difference being the different set of $\Delta \Lambda$ and ΔR steps considered.

4.3.1. Orbit raising

The results of the analysis for the orbit raising steering law are given in Table 2, where the relative error on the SMA increase achieved after one orbit, $\epsilon_{\Delta a,rel}$, is displayed for each pair of $\Delta \Lambda$ and ΔR.

Table 2 shows that the largest values for $\epsilon_{\Delta a,rel}$ are found for $\Delta \Lambda = 2$ deg and $\Delta R = 1.1^4$, whereas the smallest $\epsilon_{\Delta a,rel}$ values are achieved for intermediate values of ΔR and $\Delta \Lambda$. Nonetheless, no clear correlation between ΔR, $\Delta \Lambda$, and $\epsilon_{\Delta a,rel}$ can be derived from the results. When the relative error of 10^{-3} introduced in the atmospheric density averaging is once again used as threshold, virtually any combination of ΔR and $\Delta \Lambda$ can be adopted, including the steps $\Delta R = 1.1^4$ and $\Delta \Lambda = 2$ deg for which the least computational runtime is required both in the pre-run optimization and in-run interpolation phases. Nonetheless, since the simulations of Section 5 will be performed on Sun-synchronous orbits with values of the altitude, LTAN, and a_c different from the ones of the ACS3 mission, some contingency is considered and $\Delta R = 1.1^2 = 1.21$ and $\Delta \Lambda = 1$ deg are selected for which $\epsilon_{\Delta a,rel} = 2.7537 \cdot 10^{-5}$.

4.3.2. Inclination increase

The results for the inclination increase steering law are given in Table 3.

Table 3 shows a clear variation of $\epsilon_{\Delta i,rel}$ with ΔR and $\Delta \Lambda$. In particular, it can be noted that an increase in either ΔR or $\Delta \Lambda$
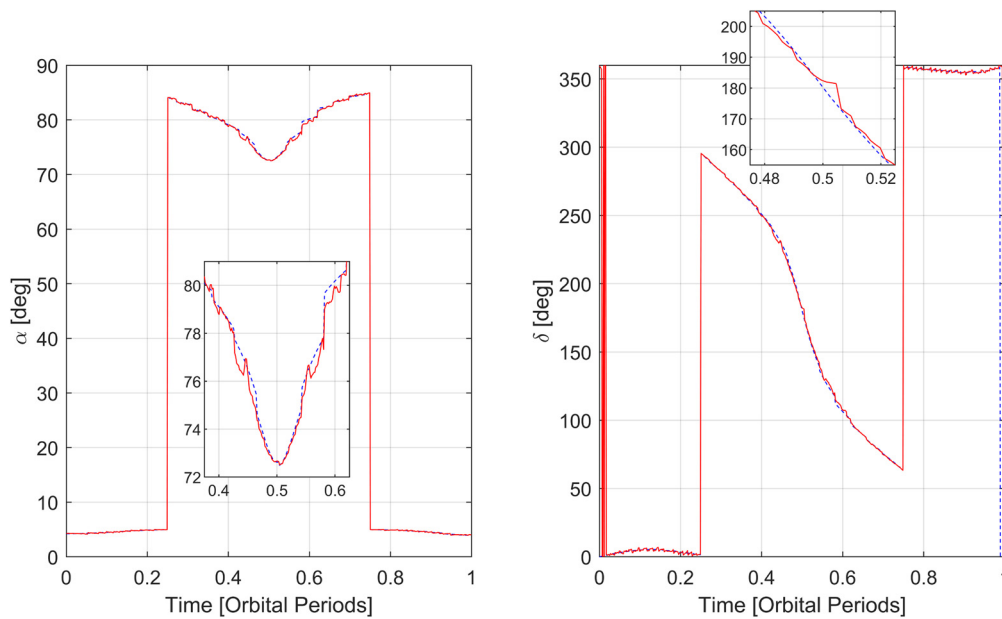
Fig. 11. Inclination increase: control profile of the reference solution (blue, dashed) and POINT solution (red, solid) over one orbital period.
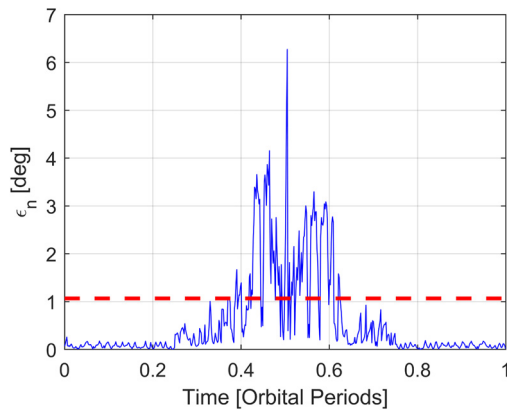
Fig. 12. Inclination increase: angular error between the sail normal directions of the reference solution and those found by the POINT method (blue, solid) and RMS of the angular error over one orbital period (red, dashed).

Fig. 14. Inclination increase: variation in inclination of the POINT solution over one orbital period.

Table 3
Relative errors on Δi for each pair of $\Delta \Lambda$ and ΔR.

$\epsilon_{\Delta i,rel} \cdot 10^{-7}$		ΔR				
		$1.1^{1/4}$	$1.1^{1/2}$	1.1	1.1^2	1.1^4
$\Delta \Lambda$ [deg]	0.1	4.6549	2.6527	9.2171	23.265	521.70
	0.2	3.9877	3.1171	8.2609	25.585	218.47
	0.5	15.403	17.043	17.518	41.719	159.00
	1.0	54.429	63.226	63.852	84.872	290.93
	2.0	304.84	365.86	290.51	410.91	523.62

of 10^{-3} introduced in the atmospheric density averaging. Therefore, using the same rationale as in Section 4.3.1, $\Delta R = 1.1^2 = 1.21$ and $\Delta \Lambda = 1$ deg are once again chosen for which $\epsilon_{\Delta i,rel} = 8.4872 \cdot 10^{-6}$.

Fig. 13. Inclination increase: relative error in Δi between the reference solution and POINT solution.

(which corresponds to a coarser grid Σ) yields a larger $\epsilon_{\Delta i,rel}$. Depending on how coarse the grid Σ is, relative errors of different magnitudes can be achieved, ranging between $2.6527 \cdot 10^{-7}$ and $5.2362 \cdot 10^{-5}$. These values are well below the relative error

4.4. Tuning of the boundaries of the acceleration ratio

The boundaries of the acceleration ratio, R_{min} and R_{max}, define when the full-dynamics optimization ($R_{min} \leq R \leq R_{max}$) is to be performed instead of the aerodynamic-based optimization ($R < R_{min}$) or SRP-based optimization ($R > R_{max}$). To determine these boundaries, multiple propagations of the ACS3 orbit are performed over one orbital period, using a range of hypothetical constant values of the atmospheric density, ρ. Based on Eq. (27) and

Fig. 15. Relative error on Δa between full-dynamics and SRP-based optimization solutions.
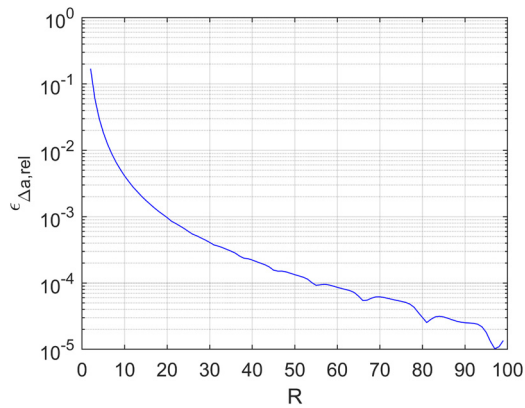
Fig. 16. Absolute error on Δa between full-dynamics and aerodynamic-based optimization solutions.

the fact that the sailcraft inertial velocity, v, remains nearly constant along one orbital revolution, the different densities uniquely determine the values of R. For each acceleration ratio, the relative difference in the final increase of a target orbital element found through the full-dynamics optimization and the aerodynamic/SRP-based optimization is computed. Finally, the values of R for which such a difference becomes smaller than a predefined threshold are taken as the boundaries R_{min} and R_{max}.

The above-mentioned analysis is performed for the orbit raising and inclination increase steering laws and the corresponding results are discussed in Sections 4.4.1 and 4.4.2, respectively. The test settings are specified in Table 1.

4.4.1. Orbit raising

The relative error between the SMA increase of the full-dynamics optimization and SRP-based optimization, $\epsilon_{\Delta a,rel}$, as a function of R is shown in the plot of Fig. 15. $\epsilon_{\Delta a,rel}$ is defined as in Eq. (33), with Δa and Δa_{ref} the increase in SMA achieved by the SRP-based optimization and full-dynamics optimization, respectively. As can be seen, $\epsilon_{\Delta a,rel}$ rapidly decreases for increasing values of R, indicating that for large acceleration ratios, the SRP AE becomes a valid approximation of the full-dynamics AE. In choosing a suitable threshold value for $\epsilon_{\Delta a,rel}$, the following should be considered. While the relative errors found in the tuning of the optimization grid in Section 4.3 were computed with respect to a reference solution found with a grid search, in this section the relative errors are defined with respect to the full-dynamics solution of the POINT method. Consequently, the relative errors $\epsilon_{\Delta a,rel}$ computed here build upon the ones found in Section 4.3. Taking this into account, and considering that an overall relative error smaller than 10^{-3} is sought, a threshold for $\epsilon_{\Delta a,rel}$ of 10^{-4} is set. As can be seen from Fig. 15, this threshold is met for $R = 55$, where $\epsilon_{\Delta a,rel} = 9.23459 \cdot 10^{-5}$. Consequently, R_{max} is set to 55.

To determine R_{min}, Fig. 16 displays the absolute error, $\epsilon_{\Delta a,abs} = \left| \Delta a - \Delta a_{ref} \right|$, between the SMA increase obtained by the aerodynamic-based optimization, Δa, and the full-dynamics optimization, Δa_{ref}, as a function of R. In this case, the absolute error is preferred as metric for the accuracy because the solution found by the aerodynamic-based optimization constantly orients the sail parallel to the wind flow, thereby yielding no variation in the SMA and a relative error of 1. As can be seen from Fig. 16, the absolute error rapidly decreases for increasing values of $1/R$, until $1/R = 1.54$ for which $\epsilon_{\Delta a,abs} = 0$. For $1/R \geq 1.54$ the aerodynamic acceleration is so dominant that the solutions found by the full-dynamics optimization and the aerodynamic-based optimization are the same. Based on this value and by including some contingency, $1/R_{min}$ is set to 4.
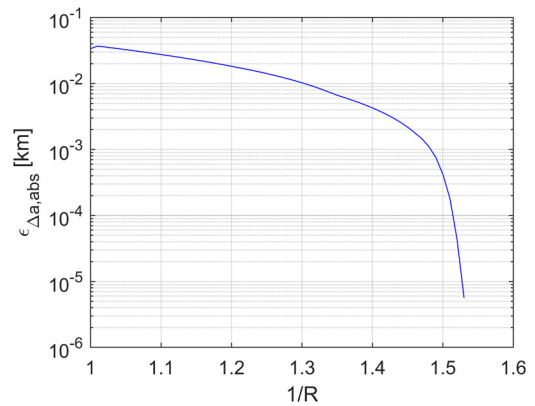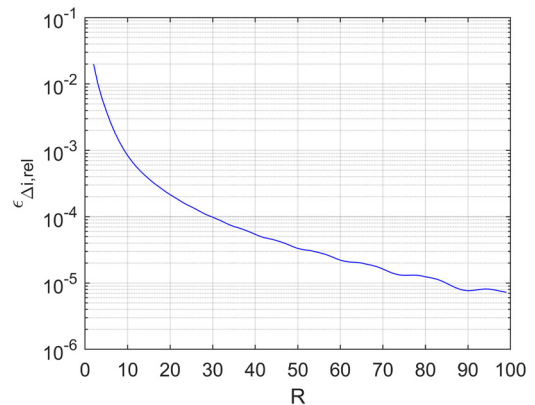
Fig. 17. Relative error on Δi between full-dynamics and SRP-based optimization solutions.

4.4.2. Inclination increase

The approach used to determine R_{min} and R_{max} for the inclination increase steering law is similar to the one used in the previous section. The only difference is that the accuracy is measured through the relative inclination error, $\epsilon_{\Delta i,rel}$, defined as per Eq. (35), where Δi and Δi_{ref} are the increases in inclination achieved by the SRP/aerodynamic-based optimization and full-dynamics optimization, respectively.

As can be seen from Fig. 17, $\epsilon_{\Delta i,rel}$ rapidly decreases for increasing values of R, thereby demonstrating the convergence of the full-dynamics AE to the SRP AE. By considering once again a maximum relative error of 10^{-4}, the acceleration ratios meeting this condition are found for $R \geq 30$. Based on this, $R_{max} = 30$ is chosen.

Fig. 18 shows that, for decreasing R values, smaller relative errors between the solutions for the full-dynamics and aerodynamic-based optimizations are obtained. Nonetheless, the values for $\epsilon_{\Delta i,rel}$ are always well above the threshold of 10^{-4}, even for very small acceleration ratios, e.g., $1/R = 100$. Without considering even smaller values for R, $1/R_{min} = 100$ is chosen as acceleration ratio boundary because values of $1/R > 100$ are highly unlikely for the analyses performed in Section 5. Such small acceleration ratios are only found for very low altitudes where the solar sail would deorbit in less than one revolution because of atmospheric drag.

5. Results and analysis

In this section, the POINT method will be used to compute the control laws to maximize the SMA or inclination change starting from different initial Earth-centered orbits and for different solar-sail characteristic accelerations and different levels of solar
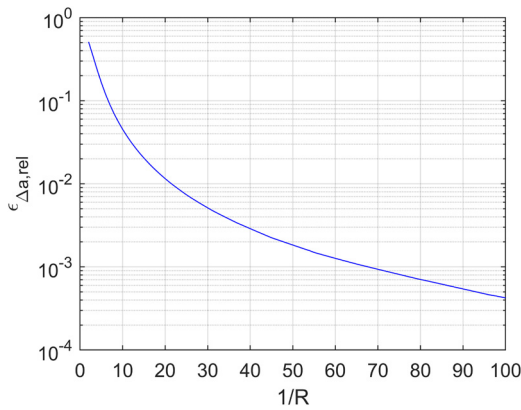
Fig. 18. Relative error on Δi between full-dynamics and aerodynamic-based optimization solutions.

activity. In this way, a wide variety of scenarios is considered and a thorough analysis of the orbit change capabilities of solar sailing for Earth-bound missions is achieved. To consider a broad range of initial conditions representative of orbits commonly used for scientific LEO missions, the analyses are performed for circular, Sun-synchronous orbits with an LTAN at 6 AM (dawn/dusk) or 12 AM (noon/midnight) and altitudes ranging between 300 km and 1000 km. The characteristic accelerations considered vary between 10^{-2} and 10^{-1} mm/s² to represent current and near-future solar-sail technology (NASA's upcoming ACS3 and NEA Scout missions will achieve solar-sail characteristic accelerations of $5.0 \cdot 10^{-2}$ and $6.3 \cdot 10^{-2}$ mm/s², respectively [43,2]). Finally, to account for the effect of solar activity on the atmospheric density, two different starting dates are considered: September 23, 2023 and September 23, 2030, corresponding to epochs of maximum and minimum solar activity, respectively. It should be noted that these dates are chosen somewhat arbitrarily within longer-duration periods of solar maximum and minimum activity and correspond to the autumn equinoxes, for which the Sun "orbits" in the Earth's equatorial plane. Other dates within the periods of solar maximum/minimum can of course be considered, which would then correspond to slightly different orientations of the science orbit with respect to the Sun and, therefore, would lead to slightly different results of the analyses.

For each scenario, an orbit propagation of 10 days is performed using Matlab®'s *ode45* integrator, with absolute and relative tolerances of 10^{-12}. Consistent with the values obtained in Section 4, the averaged NRLMSISE-00 atmospheric density is used with SpO = 25 and NpS = 4. The POINT optimization method uses an optimized grid Σ found through $\Delta\Lambda = 1$ deg and $\Delta R = 1.21$. Finally, the acceleration ratio domains considered are $R \in [1/4, \ 55]$ and $R \in [1/100, \ 30]$ for the orbit raising and inclination increase steering laws, respectively.

5.1. Orbit raising

The results for the parametric analyses performed for the orbit raising steering law appear in Fig. 19. The four plots display the increase in SMA achieved after 10 days for different combinations of LTAN and solar activity. Each plot shows 10 curves for 10 different values of the characteristic acceleration. The figure shows that, independently of the LTAN, the solar activity determines the minimum altitude for which orbit raising is still possible. This minimum altitude is approximately equal to 450 and 600 km for minimum and maximum solar activity, respectively, and therefore demonstrates the orbit raising capabilities of solar sails above such altitudes. The plots also show that the effect of a different solar activity on Δa becomes negligible at high altitudes, as the curves

asymptotically tend to the same values. At such high altitudes, the aerodynamic drag becomes negligible and similar SMA increases are found even for largely different solar activities. Comparison of the plots for different LTAN values and the same solar activity shows that the effect of changing the LTAN from 6AM (dawn/dusk) to 12AM (noon/midnight) reduces the SMA increase due to the presence of eclipses for a noon/midnight orbit.

The results in Fig. 19 for $a_c = 5.0 \cdot 10^{-2}$ mm/s² are combined in Fig. 20 to gain further insights in the ranges of achievable SMA increase. For example, if one considers a specific LTAN, the two curves for minimum and maximum solar activity enclose the region of maximum SMA increase for any solar activity. A specific example is given by the two marks that represent the ACS3 mission with a simulation start date of July 1st, 2022. This date corresponds to an intermediate solar activity and, as such, the Δa values achieved for the ACS3 mission lie well within the above-mentioned region. Alternatively, the curves for a fixed solar activity but with different LTANs can be considered. Since LTANs at 6AM and 12AM represent the orbits with the shortest and longest eclipsing time, respectively, any initial orbit with an LTAN different from 6AM or 12AM will show an SMA increase within the region enclosed by these two curves. Fig. 20 shows that the largest SMA increases are achieved at solar minimum and for an LTAN at 6AM, whereas the smallest values for Δa are achieved at solar maximum and for an LTAN at 12AM. These two curves correspond to the overall best and worst orbit raising scenarios. For any circular, Sun-synchronous orbit the achievable increase in SMA is always enclosed by these curves.

The results in Fig. 19 and Fig. 20 can be used to conduct the preliminary design of solar-sail LEO missions. In fact, although the results are given only for a propagation time of 10 days, the achievable SMA increase for longer propagation times can be retrieved from the same results by consulting the plots in an iterative fashion: consider a given initial altitude, h_0, with an SMA increase Δa_0, then the same plot can be reused starting from a new altitude $h_1 = h_0 + \Delta a_0$ to retrieve Δa_1, which in turn is used to define h_2 and so forth. At each iteration of this process the mission duration increases by 10 days, so that the iterations can be stopped until the desired mission duration is obtained.

5.2. Inclination increase

The results of the parametric analyses for the inclination increase steering law appear in Fig. 21. The truncation of the curves at low altitude is due to a rapid loss in altitude when increasing the inclination under the effects of atmospheric drag. The orbit propagation is stopped when an altitude lower than 100 km is reached within 10 days. As can be seen, the altitude at which this condition occurs ranges between 400 and 650 km and depends on the characteristic acceleration, solar activity, and LTAN. An interesting trend which can be appreciated in all four plots of Fig. 21 is the steep gradient in the inclination increase for decreasing altitudes: when lowering the orbital altitude, not only drag increases, but also the aerodynamic lift, which provides the out-of-plane acceleration used to change the inclination. At higher altitudes, no significant change in the inclination increase as a function of altitude can be observed. Conversely, a strong correlation between the inclination increase and the solar-sail characteristic acceleration can be noted.

Similar to Fig. 20 for the orbit raising case, Fig. 22 displays the variation in inclination increase for a characteristic acceleration of $a_c = 5 \cdot 10^{-2}$ mm/s², for minimum and maximum solar activity and LTANs at 6AM and 12AM. For increasing values of h_0, the results for the solar minimum case and solar maximum case converge to the same values. This is because the atmospheric density decreases and the inclination increase is produced solely by the
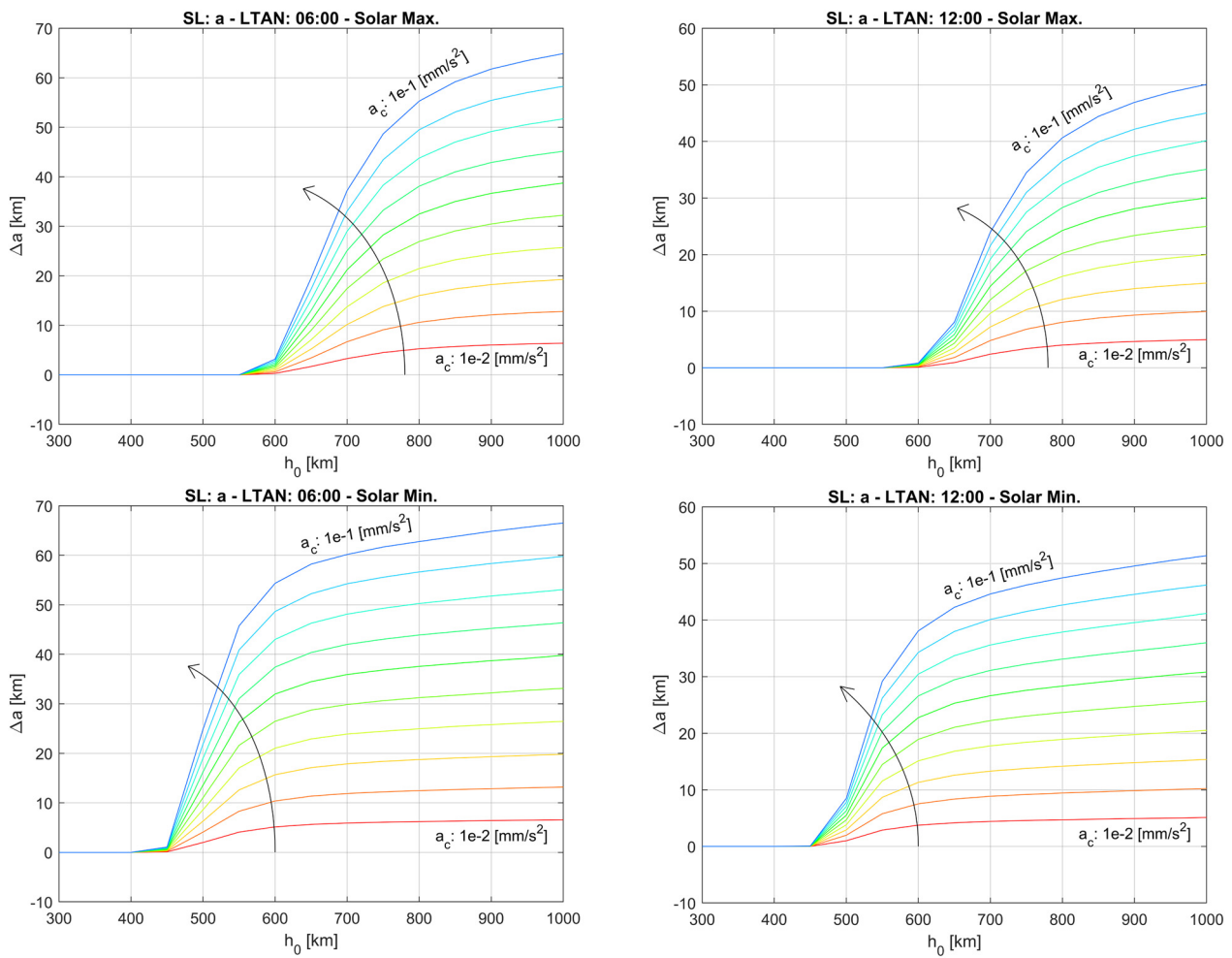
Fig. 19. Orbit raising steering law: SMA increase as a function of the initial altitude and solar-sail characteristic acceleration for different LTAN values and solar activities. The characteristic acceleration increases in the direction of the arrow from 10^{-2} to 10^{-1} mm/s^2 with a step size of 10^{-2} mm/s^2.
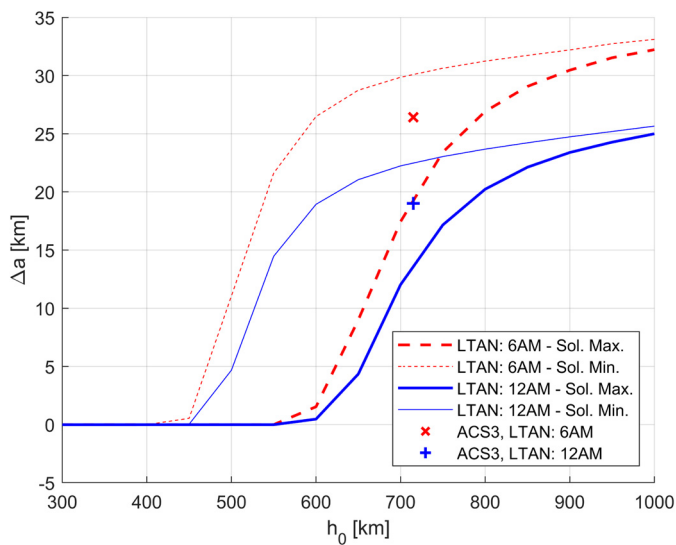
Fig. 20. Orbit raising steering law: SMA increase for $a_c = 5 \cdot 10^{-2}$ mm/s^2.

SRP acceleration, which is equal in both cases. Fig. 22 also shows the inclination increases achievable by the ACS3 missions at an intermediate solar activity. As can be seen, the values for Δi fall slightly below or above the regions enclosed by the minimum and maximum solar activity. By further analyzing these results, it was

found that these differences are due to the simulation start date of July 1st, 2022 which results in a different orientation of the ACS3's initial orbit with respect to the Sun than at the autumn equinox, and hence different values for Δi.

6. Conclusions

In this article a novel method to optimize Earth-bound solar-sail orbits in the presence of atmospheric drag has been presented and employed on a wide variety of scenarios. To reduce the computational effort required, an averaged atmospheric density model has been introduced and its performance has been tested, both with respect to its accuracy and runtime. The optimal control problem has been formulated and thoroughly analyzed for three different dynamical regimes. These are the solar radiation pressure (SRP)-dominated regime, the aerodynamic drag-dominated regime, and the full-dynamics (SRP + drag) regime, for which it has been shown that the optimal control problem is independent of the solar-sail loading parameter. To solve the full-dynamics optimal control problem, the POINT optimization method has been developed, which is based on a pre-run optimization phase and in-run interpolation phase. The pre-run optimization phase takes place before the trajectory propagation and aims to solve the optimal control problem for a broad range of scenarios, in order to store the corresponding optimal sail normal directions. Afterwards, the in-run interpolation of the optimal sail normal directions takes place at each integration time step during the propagation. All
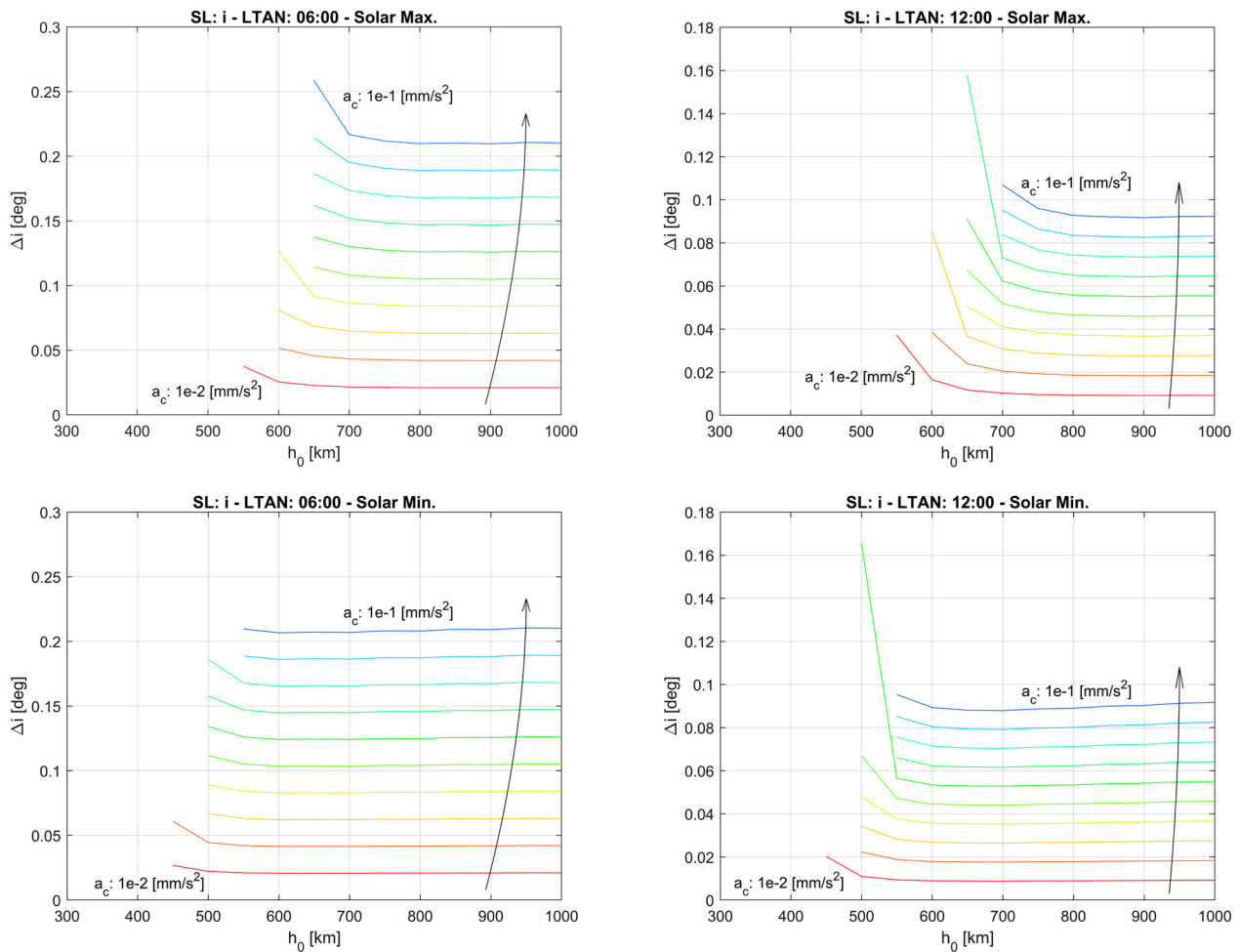
Fig. 21. Inclination increase steering law: inclination increase as a function of the initial altitude and solar-sail characteristic acceleration for different LTAN values and solar activities. The characteristic acceleration increases in the direction of the arrow from 10^{-2} to 10^{-1} mm/s^2 with a step size of 10^{-2} mm/s^2.
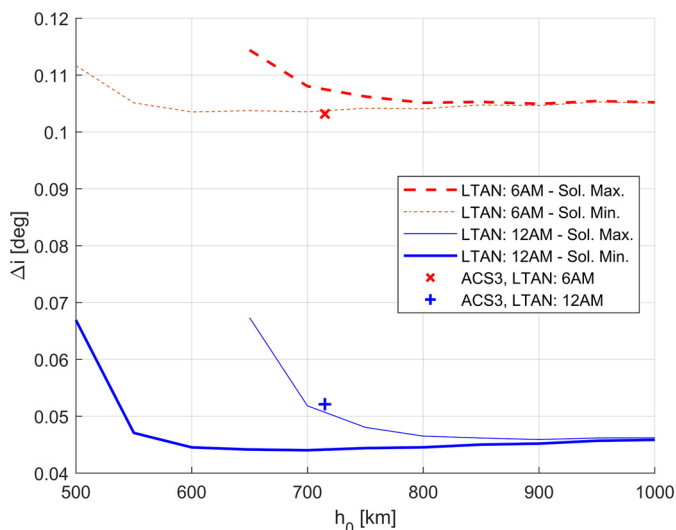
Fig. 22. Inclination increase steering law: inclination increase for $a_c = 5 \cdot 10^{-2}$ mm/s^2.

parameters used by the POINT method have been tuned and a validation test has been performed to demonstrate the accuracy and global validity of the optimal solutions found. The POINT method has been applied to an orbit raising steering law and inclination increase steering law on NASA's upcoming ACS3 mission and a

range of other circular, Sun-synchronous orbits, differing from each other in the local time of the ascending node, the altitude, and the solar-sail characteristic acceleration. The results of the analyses show that the minimum altitude for which orbit raising is achievable varies between 450 and 600 km and strongly depends on the solar activity, while the local time of the ascending node affects the magnitude of the altitude increase. The inclination increase steering law proved to be unsuited for orbits with altitudes below $400 \div 650$ km, as the sailcraft tends to deorbit rapidly. Conversely, at high altitudes, increases in inclination are achievable, with their magnitude depending largely on the solar-sail characteristic acceleration.

Declaration of competing interest

The authors declare that they have no known competing financial interests or personal relationships that could have appeared to influence the work reported in this paper.

Acknowledgements

References

[1] C.R. McInnes, Solar Sailing - Technology, Dynamics and Mission Applications, Springer, 2004.

[2] D.A. Spencer, L. Johnson, A.C. Long, Solar sailing technology challenges, Aerosp. Sci. Technol. 93 (2019), https://doi.org/10.1016/j.ast.2019.07.009.

[3] M. Macdonald, C.R. McInnes, Solar sail science mission applications and advancement, Adv. Space Res. (2011) 1702–1716, https://doi.org/10.1016/j.asr.2011.03.018.

[4] B. Dachwald, Optimal solar-sail trajectories for missions to the outer solar system, J. Guid. Control Dyn. 28 (6) (2005) 1187–1193, https://doi.org/10.2514/1.13301.

[5] M. Whorton, A. Heaton, R. Pinson, G. Laue, C. Adams, NanoSail-D: the first flight demonstration of solar sails for nanosatellites, in: AIAA/USU Conference on Small Satellites, Logan, Utah, 2008.

[6] M. Macdonald, Advances in Solar Sailing, Springer, 2014, pp. 95–113.

[7] B. Betts, B. Nye, E. Greeson, et al., LightSail 1 mission results and public outreach strategies, in: Proceedings of the 4th International Solar Sailing Symposium, Kyoto, Japan, 2017.

[8] D.A. Spencer, B. Betts, J.M. Bellardo, A. Diaz, B. Plante, J.R. Mansell, The LightSail 2 solar sailing technology demonstration, Adv. Space Res. 67 (9) (2021) 2878–2889, https://doi.org/10.1016/j.asr.2020.06.02.

[9] W.K. Wilkie, J.M. Fernandez, O.R. Stohlman, et al., An overview of the NASA advanced composite solar sail (ACS3) technology demonstration project, in: AIAA Scitech 2021 Forum, 2021.

[10] M. Macdonald, C.R. McInnes, Analytical control laws for planet-centered solar sailing, J. Guid. Control Dyn. 28 (5) (2005) 1038–1048, https://doi.org/10.2514/1.11400.

[11] C.R. McInnes, M. Macdonald, V. Angelopolous, D. Alexander, GEOSAIL: exploring the geomagnetic tail using a small solar sail, J. Spacecr. Rockets 38 (4) (2001) 622–629, https://doi.org/10.2514/2.3727.

[12] M. Macdonald, C.R. McInnes, Realistic Earth escape strategies for solar sailing, J. Guid. Control Dyn. 28 (2) (2005) 315–323, https://doi.org/10.2514/1.5165.

[13] V. Coverstone, J.E. Prussing, Technique for escape from geosynchronous transfer orbit using a solar sail, J. Guid. Control Dyn. 26 (4) (2003) 628–634, https://doi.org/10.2514/2.5091.

[14] G. Mengali, A.A. Quarta, Earth escape by ideal sail and solar-photon thrustor spacecraft, J. Guid. Control Dyn. 27 (6) (2004) 1105–1108, https://doi.org/10.2514/1.10637.

[15] A. De Iuliis, F. Ciampa, L. Felicetti, M. Ceriotti, Sailing with solar and planetary radiation pressure, in: Proceedings of ISSS 2019: 5th International Symposium on Solar Sailing, Aachen, Germany, 2019.

[16] A. Barles, M. Ceriotti, F. Ciampa, L. Felicetti, An optimal steering law for sailing with solar and planetary radiation pressure, Aerosp. Sci. Technol. 118 (2021), https://doi.org/10.1016/j.ast.2021.107051.

[17] G. Mengali, A.A. Quarta, Near-optimal solar-sail orbit-raising from low Earth orbit, J. Spacecr. Rockets 42 (5) (2005) 954–958, https://doi.org/10.2514/1.14184.

[18] T.O. Morgan, The inclination change for solar sails and low Earth orbit, Adv. Astronaut. Sci. (1979) 559–573.

[19] V. Stolbunov, M. Ceriotti, C. Colombo, C.R. McInnes, Optimal law for inclination change in an atmosphere through solar sailing, J. Guid. Control Dyn. 36 (5) (2013) 1310–1323, https://doi.org/10.2514/1.59931.

[20] P.D. Fieseler, A method for solar sailing in a low Earth orbit, Acta Astronaut. 43 (9–10) (1998) 531–541, https://doi.org/10.1016/S0094-5765(98)00175-1.

[21] N. Miguel, C. Colombo, Planar orbit and attitude dynamics of an Earth-orbiting solar sail under J2 and atmospheric drag effects, in: AAS/AIAA Astrodynamics Specialist Conference, Snowbird, Utah, USA, 2018.

[22] N. Miguel, C. Colombo, Deorbiting spacecraft with passively stabilised attitude using a simplified quasi-rhombic-pyramid sail, Adv. Space Res. 67 (9) (2021) 2561–2576, https://doi.org/10.1016/j.asr.2020.03.028.

[23] C. Colombo, A. Rossi, F. Dalla Vedova, V. Braun, B. Bastida Virgili, H. Krag, Drag and solar sail deorbiting: Re-entry time versus cumulative collision probability, in: 68th International Astronautical Congress, Adelaide, Australia, 2017.

[24] A. Ionel, Deorbiting upper-stages in LEO at EOM using solar sails, Incas Bulletin 9 (2) (2017) 117–132, https://doi.org/10.13111/2066-8201.2017.9.2.9.

[25] L. Niccolai, A.A. Quarta, G. Mengali, Analytical solution of the optimal steering law for non-ideal solar sail, Aerospace Science and Technology 62 (2017) 11–18, https://doi.org/10.1016/j.ast.2016.11.031.

[26] B. Wie, Solar sail attitude control and dynamics, part 1, J. Guid. Control Dyn. 27 (4) (2004) 526–535.

[27] G. Mengali, A.A. Quarta, Solar sail trajectories with piecewise-constant steering laws, Aerosp. Sci. Technol. 13 (8) (2009) 431–441, https://doi.org/10.1016/j.ast.2009.06.007.

[28] L. Rios-Reyes, Solar Sails: Modeling, Estimation, and Trajectory Control, University of Michigan, Ann Arbor, Michigan, USA, 2006.

[29] S. Firuzi e, S. Gong, Gradient-index solar sail and its optimal orbital control, Aerosp. Sci. Technol. 119 (107103) (2021), https://doi.org/10.1016/j.ast.2021.107150.

[30] C. Bianchi, L. Niccolai, G. Mengali e, A.A. Quarta, Collinear artificial equilibrium point maintenance with a wrinkled solar sail, Aerosp. Sci. Technol. 119 (107150) (2021), https://doi.org/10.1016/j.ast.2021.107150.

[31] S. Firuzi e, S. Gong, Refractive sail and its applications in solar sailing, Aerosp. Sci. Technol. 77 (2018) 362–372, https://doi.org/10.1016/j.ast.2018.03.016.

[32] J.R. Wertz, W.J. Larson, Space Mission Analysis and Design, Microcosm Press/Kluwer Academic Publishers, El Segundo, California, USA, 2005.

[33] C.R. Ortiz Longo, S.L. Rickman, Method for the Calculation of Spacecraft Umbra and Penumbra Shadow Terminator Points, NASA Center for AeroSpace Information, Linthicum Heights, 1995.

[34] P. Kelly, R. Bevilacqua, An optimized analytical solution for geostationary debris removal using solar sails, Acta Astronaut. 162 (2019) 72–86, https://doi.org/10.1016/j.actaastro.2019.05.055.

[35] R.S. Nerem, F.J. Lerch, J.A. Marshall, E.C. Pavlis, B.H. Putney, B.D. Tapley, R.J. Eanes, J.C. Ries, B.E. Schutz, C.K. Shum, M.M. Watkins, S.M. Klosko, J.C. Chan, S.B. Luthcke, G.B. Patel, N.K. Pavlis e, et al., Gravity model development for TOPEX/POSEIDON: joint gravity models 1 and 2, J. Geophys. Res. 99 (C12) (1994) 24,421–24,447, https://doi.org/10.1029/94JC01376.

[36] J.A. Storch, Aerodynamic disturbances on spacecraft in free-molecular flow, in: The Aerospace Corporation, 2002.

[37] P.C. Hughes, Spacecraft Attitude Dynamics, Dover Publications Inc., New York, 2004.

[38] J.M. Picone, A.E. Hedin, D.P. Drob, NRLMSISE-00 empirical model of the atmosphere: statistical comparisons and scientific issues, J. Geophys. Res. 107 (A12) (2002), https://doi.org/10.1029/2002JA009430.

[39] R.R. Bate, D.D. Mueller, J.E. White, Fundamentals of Astrodynamics, Dover Publications, Inc., New York, 1971.

[40] D. Shepard, A two-dimensional interpolation for irregularly-spaced data function, in: 23rd ACM National Conference, 1968.

[41] G.P. Styan, Hadamard products and multivariate statistical analysis, Linear Algebra Appl. 6 (1973) 217–240, https://doi.org/10.1016/0024-3795(73)90023-2.

[42] F. Nielsen, Hierarchical clustering, in: Introduction to HPC with MPI for Data Science, Springer International Publishing, 2016, pp. 195–211.

[43] J. Pezent, R. Soon, A. Heaton, High-fidelity contingency trajectory design and analysis for NASA's near-Earth asteroid (NEA) scout solar sail mission, Acta Astronaut. 159 (2019) 385–396, https://doi.org/10.1016/j.actaastro.2019.03.050.

[44] NASA Marshall Space Flight Center, Marshall solar cycle forecast, https://www.nasa.gov/msfcsolar/archivedforecast. (Accessed 15 December 2021).